



HAL
open science

Seismic Crustal Structure and Morphotectonic Features Associated With the Chain Fracture Zone and Their Role in the Evolution of the Equatorial Atlantic Region

Milena Marjanović, Satish C. Singh, Emma P. M. Gregory, Ingo Grevemeyer, Kevin Growe, Zhikai Wang, Venkata Vaddineni, Muriel Laurencin, Hélène Carton, Laura Gómez de La Peña, et al.

► To cite this version:

Milena Marjanović, Satish C. Singh, Emma P. M. Gregory, Ingo Grevemeyer, Kevin Growe, et al.. Seismic Crustal Structure and Morphotectonic Features Associated With the Chain Fracture Zone and Their Role in the Evolution of the Equatorial Atlantic Region. *Journal of Geophysical Research : Solid Earth*, 2020, 125, p.1535-1581. 10.1029/2020JB020275 . insu-03584469

HAL Id: insu-03584469

<https://insu.hal.science/insu-03584469>

Submitted on 22 Feb 2022

HAL is a multi-disciplinary open access archive for the deposit and dissemination of scientific research documents, whether they are published or not. The documents may come from teaching and research institutions in France or abroad, or from public or private research centers.

L'archive ouverte pluridisciplinaire **HAL**, est destinée au dépôt et à la diffusion de documents scientifiques de niveau recherche, publiés ou non, émanant des établissements d'enseignement et de recherche français ou étrangers, des laboratoires publics ou privés.



Distributed under a Creative Commons Attribution - NonCommercial - NoDerivatives 4.0 International License

JGR Solid Earth



RESEARCH ARTICLE

10.1029/2020JB020275

Key Points:

- Fracture zones are represented by close to normal crustal thickness (~5 km) that we attribute to the mechanism of lateral dike propagation
- Major reorganization in plate motion represents a predominant factor in building transverse ridge at the Chain Fracture Zone
- The analysis of our seismic data sets and interdisciplinary observations define lower-order tectonomagmatic segmentation of the ridge axis

Supporting Information:

- Supporting Information S1

Correspondence to:

M. Marjanović,
marjanovic@ippg.fr

Citation:

Marjanović, M., Singh, S. C., Gregory, E. P. M., Grevemeyer, I., Growe, K., Wang, Z., et al. (2020). Seismic crustal structure and morphotectonic features associated with the Chain Fracture Zone and their role in the evolution of the equatorial Atlantic region. *Journal of Geophysical Research: Solid Earth*, 125, e2020JB020275. <https://doi.org/10.1029/2020JB020275>

Received 28 MAY 2020

Accepted 1 SEP 2020

Accepted article online 7 SEP 2020

Seismic Crustal Structure and Morphotectonic Features Associated With the Chain Fracture Zone and Their Role in the Evolution of the Equatorial Atlantic Region

Milena Marjanović¹ , Satish C. Singh¹ , Emma P. M. Gregory¹ , Ingo Grevemeyer² , Kevin Growe³, Zhikai Wang¹ , Venkata Vaddineni¹, Muriel Laurencin¹ , Hélène Carton¹ , Laura Gómez de la Peña² , and Christian Filbrandt²

¹Université de Paris, Institut de Physique du Globe de Paris, CNRS, Paris, France, ²GEOMAR Helmholtz Centre of Ocean Research Kiel, RD4—Marine Geodynamics, Kiel, Germany, ³Applied Geophysics Program, TU Delft, ETH Zürich, RWTH Aachen, Aachen, Germany

Abstract Oceanic transform faults and fracture zones (FZs) represent major bathymetric features that keep the records of past and present strike-slip motion along conservative plate boundaries. Although they play an important role in ridge segmentation and evolution of the lithosphere, their structural characteristics, and their variation in space and time, are poorly understood. To address some of the unknowns, we conducted interdisciplinary geophysical studies in the equatorial Atlantic Ocean, the region where some of the most prominent transform discontinuities have been developing. Here we present the results of the data analysis in the vicinity of the Chain FZ, on the South American Plate. The crustal structure across the Chain FZ, at the contact between ~10 and 24 Ma oceanic lithosphere, is sampled along seismic reflection and refraction profiles. We observe that the crustal thickness within and across the Chain FZ ranges from ~4.6–5.9 km, which compares with the observations reported for slow-slipping transform discontinuities globally. We attribute this presence of close to normal oceanic crustal thickness within FZs to the mechanism of lateral dike propagation, previously considered to be valid only in fast-slipping environments. Furthermore, the combination of our results with other data sets enabled us to extend the observations to morphotectonic characteristics on a regional scale. Our broader view suggests that the formation of the transverse ridge is closely associated with a global plate reorientation that was also responsible for the propagation and for shaping lower-order Mid-Atlantic Ridge segmentation around the equator.

1. Introduction

An oceanic transform fault (TF) that separates ridge segments, also known as a first-order tectonic discontinuity, represents a conservative plate boundary along which two plates move past each other, that is, exhibit strike-slip motion (Kearey & Vine, 2002; Menard, 1967; Wilson, 1965). The traces of this transform boundary can be followed in the older lithosphere for several thousands of kilometers, beyond the ridge-transform intersection (RTI), following arcs of small circles on the Earth's surface (Bonatti & Crane, 1982; Morgan, 1968), and are identified as fracture zones (FZs). By definition, the FZ domains do not represent a plate boundary per se but an intraplate juxtaposition of two lithospheric blocks of different ages belonging to the same tectonic plate (DeLong et al., 1977; Menard & Atwater, 1969). The older of these lithospheric blocks is highly deformed as it carries the record of its passage through the TF domain (DeLong et al., 1977; Karson & Dewey, 1978); the younger lithospheric block is welded to the older and colder lithospheric block beyond the RTI (Karson & Dick, 1983). However, the prevailing view that FZs represent inactive intraplate contact has been questioned in the past (e.g., Batiza, 1981, 1982; Lowrie et al., 1986; Vogt, 1974). The discussion has been revived recently as a number of earthquakes of nonnegligible magnitudes have been recorded in FZs (e.g., Antolik et al., 2006; Bohnenstiehl et al., 2004; Lay, 2019), including the 2016 earthquake ($M = 5.2$), which took place ~180 km east of the eastern RTI of the Chain TF (catalog of the U.S. Geological Survey 2016). Regardless of the presence/absence of tectonic activity, an FZ domain, together with its parent TF domain, can be referred to as a transform discontinuity system.

©2020. The Authors.

This is an open access article under the terms of the Creative Commons Attribution-NonCommercial-NoDerivs License, which permits use and distribution in any medium, provided the original work is properly cited, the use is non-commercial and no modifications or adaptations are made.

Much of what we know about the nature of oceanic crust within transform discontinuity systems came from a large number of active-source seismic refraction (and some reflection) experiments conducted in the 1980s in slow-spreading (20–50 mm/yr) environments (e.g., Ambos & Hussong, 1986; Calvert & Potts, 1985; Cormier et al., 1984; Detrick & Purdy, 1980; Detrick et al., 1982, 1993; Fox et al., 1976; Minshull et al., 1991; Mutter et al., 1984; Potts, Calvert, et al., 1986; Potts, White, et al., 1986; Sinha & Loudon, 1983; White et al., 1990; Whitmarsh & Calvert, 1986). A global notion resulting from these studies is that the subsurface within slow-slipping transform discontinuity systems (including FZ domains) is represented by thin, highly fractured and altered crust, often with partially or entirely absent gabbroic layer (e.g., Cormier et al., 1984; Detrick et al., 1982, 1993; Detrick & Purdy, 1980; Whitmarsh & Calvert, 1986). This common view of thinner crust within slow-slipping transform discontinuity systems is reasonable under the assumption that the accretion along slow-spreading mid-ocean ridge segments is controlled by 3-D segment-centered mantle upwelling (Bell & Buck, 1992; Lin et al., 1990), which was established by previous studies (e.g., Detrick et al., 1995; Gregg et al., 2007, 2009; Kuo & Forsyth, 1988; Lin & Phipps Morgan, 1992; Tolstoy et al., 1993).

Besides examining crustal properties within the transform discontinuity systems, researchers have also been intrigued by the associated morphotectonic features (Maia, 2018, and references therein). One of the characteristic features found foremost within the slow-slipping transform discontinuity system environments is a transverse ridge with a well-developed uplifted morphology. Transverse ridges are represented by elongated, narrow, and elevated ridge-like structure running parallel to the walls of the transform discontinuity systems (e.g., Bonatti, 1978). Most of them are mapped along the older side of the lithospheric block of the FZ domain (e.g., Abrams et al., 1988; Bonatti, 1978; Kastens et al., 1998; Tucholke & Schouten, 1988). Although their presence and characteristic seafloor morphology were identified and described in great detail in the early stage of seafloor exploration, their origin was extensively debated (Abrams et al., 1988; Cannat et al., 1991; Kastens et al., 1998). A number of hypotheses, from constructional volcanism, serpentinite diapirism, and thermal, viscodynamic to kinematic forces, were proposed (e.g., Abrams et al., 1988; Bonatti, 1978; Bonatti et al., 1994; Cannat et al., 1991; Kastens et al., 1998; Pockalny et al., 1996), but strong consensus on the predominant mechanism was not attained.

Finally, between two large-scale, first-order tectonic discontinuities (i.e., TFs), the presence of another type of lower-order (i.e., second-order) tectonic discontinuity was identified from its expression in bathymetry (e.g., Carbotte et al., 2015; Macdonald et al., 1991). At slow-spreading centers, this type of discontinuity is termed as a nontransform offset or NTO (Carbotte et al., 2015; Macdonald et al., 1991; Sempéré et al., 1993; Spencer et al., 1997; Thibaud et al., 1998). On the seafloor, the NTOs can be observed as (1) a step-sided ridge bounded by faults (with 15–30 km offset), (2) an oblique shear zone, and (3) an offset in the volcanic axis (Sempéré et al., 1993). Furthermore, they can often be associated with prominent off-axis traces that witness their longevity of several millions of years (Macdonald et al., 1991). In some cases the off-axis traces can be represented by V-shaped discordant zones, that is, pseudofaults (Carbotte et al., 2015), which result from the propagation of the tip of the advancing ridge segment at the expense of the adjacent, dying segment (e.g., Hey et al., 1980; Hey & Vogt, 1977; Kleinrock & Hey, 1989). However, the subsurface characteristics of these features are still largely unknown.

Conducting an interdisciplinary study in the region of the equatorial Atlantic Ocean offers a unique opportunity to inspect the characteristics of large transform discontinuity systems, St. Paul, Romanche, and Chain, and examine their role in the morphotectonic evolution of the area. While the first two transform discontinuity systems have been subjects of a number of interdisciplinary studies in the past (e.g., Bonatti, 1978; Bonatti et al., 1994, 2001; Bonatti, Ligi, Borsetti, et al., 1996; Bonatti, Ligi, Carrara, et al., 1996; Ligi et al., 2002; Maia, 2018; Maia et al., 2016), little is known about the Chain transform discontinuity system, which can be followed continuously to the continental margins of the African (Nubian) and South American Plates (Figure 1a). Here, we focus on examining the crustal characteristics of the Chain FZ using a combination of active-source seismic reflection and refraction data sets as well as global and local bathymetry and gravity data sets. In particular, we investigate crustal thickness variations across the FZ and compare our results with those obtained for other transform discontinuity systems (both fracture and transform domains) within slow-slipping environments. The crustal structure is also examined across a pseudofault resulting from a ridge segment propagation at an NTO present south of the Chain TF. Furthermore, we identify and describe morphotectonic features of the bounding ridge segments in the area centered

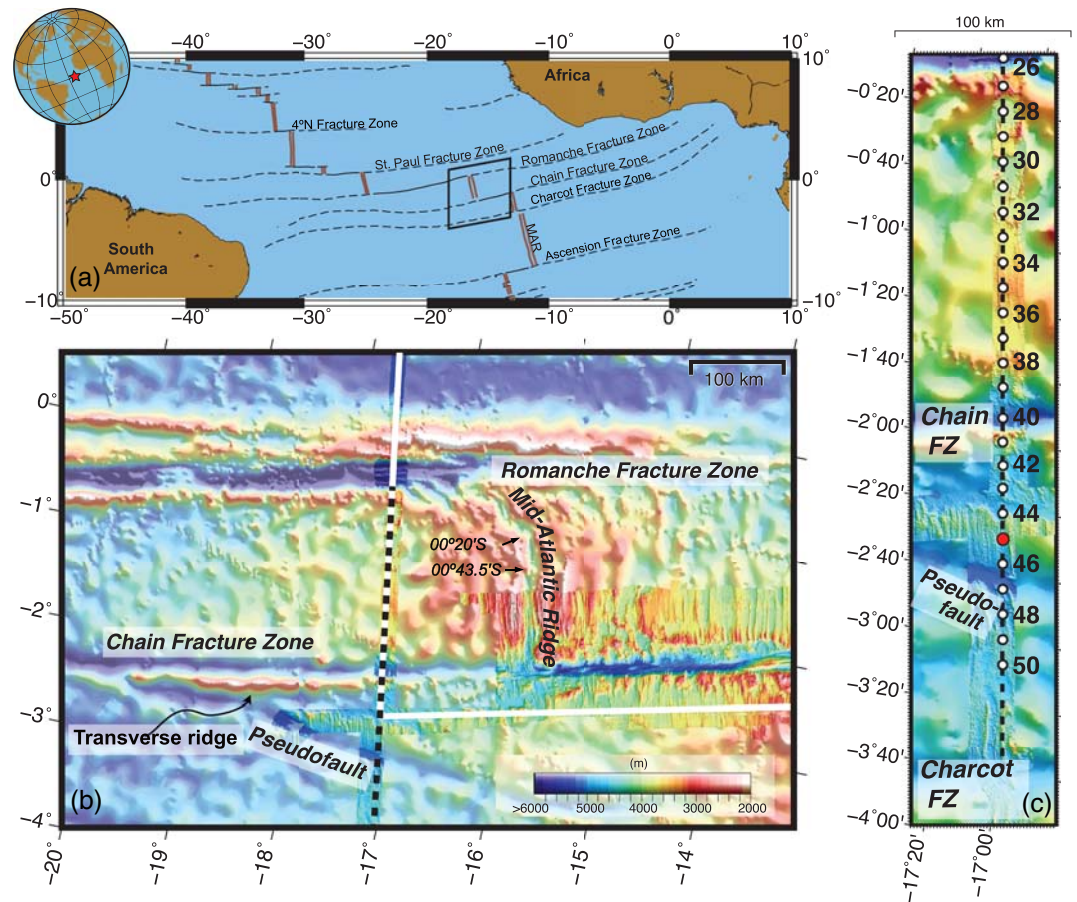


Figure 1. Survey area. (a) Global tectonic setting of the equatorial Atlantic (red star in the globe inset). The double lines in brown indicate the axial zone of the Mid-Atlantic Ridge (MAR). The solid and dashed black lines outline the tracks of transform faults and fracture zones, respectively. The plate boundary model (Bird, 2003) is for illustration purposes. The black box indicates the location of the regional map of the survey area shown in panel. (b) The bathymetry map is obtained by merging high-resolution bathymetry grids collected during Pi-LAB (Harmon et al., 2018), LITHOS (Grevemeyer et al., 2019), and ILAB-SPARC (Marjanović et al., 2019) experiments. This combined bathymetry grid is superimposed on a global lower-resolution grid (GEBCO Compilation Group), which is masked for better visibility of the high-resolution data. The main structural features are indicated on the map. The black dashed line shows the part of the ocean bottom seismometer (OBS) and multichannel seismic (MCS) data collected during ILAB-SPARC survey that are included in this study. The white line shows the location of the MCS line collected in 2015 (Marjanović et al., 2015). The arrows indicate a large-scale segmentation of the MAR we identified (see text). (c) The portion of the OBS line used in this study showing the locations of OBS instruments from 26 to 50 in white circles (only even numbers of the OBSs are labeled). The red circle shows the location of OBS 34, the record of which is displayed in Figure 4. All the panels are produced using GMT.

around the Chain TF and associated NTOs and interpret them in the context of crustal accretion processes. Finally, we investigate the possible mechanisms for the formation of a transverse ridge observed ~120 km west of the western RTI.

2. Study Area

The study area is centered around the Chain FZ; in the north-south direction it extends from the south of the Romanche TF to just north of the Charcot FZ (Figure 1b). Regionally, it belongs to the equatorial Atlantic Zone, which started opening in the Early Cretaceous, ~100–140 Ma (Bonatti, Ligi, Borsetti, et al., 1996; Gasperini et al., 2001; Granot & Dyment, 2015; Larson & Ladd, 1979; Moulin et al., 2010) and developed some of the most prominent transform discontinuity systems on our planet (Figure 1a). It was only recently that a high-resolution bathymetry and potential field (magnetic and gravity) data sets were obtained around

the 300 km long Chain TF offset, which provided first-order insights on its tectonic history (Harmon et al., 2018). Within the TF domain, four positive flower structures and en échelon fault scarps were identified. However, the overall conclusion is that compressional and extensional features within the Chain TF are less pronounced when compared to the Romanche and St. Paul TFs located directly to the north. The current orientations and some of the tectonic characteristics of the St. Paul and Romanche transform discontinuity systems (e.g., construction of islets within St. Paul: Maia et al., 2016) seem to be inherited from a 5° counter-clockwise rotation that took place ~11 Ma ago due to the plates readjustment (Bonatti et al., 2005). However, by examining magnetic data, Harmon et al. (2018) suggested that the tectonic features in the Chain TF due to this 11 Ma plate rotation event are more subdued. This observation led the authors to speculate that the Chain TF could be at the southern limit of this deformational front. Finally, the newly collected magnetic data (Harmon et al., 2018) helped improve reconstruction of crustal age for the last 15–20 Myr, inferring asymmetric separation of the African and South American Plates during the last ~3 Myr with the South American Plate moving away slightly slower (15.7 mm/yr) than the African Plate (18.2 mm/yr) relative to the ridge axis.

3. Data and Methods

The data were collected as a result of a community effort to investigate properties of the oceanic lithosphere spanning a wide range of lithospheric ages. The frame for working in the area was set up by an active-source seismic reflection survey employing an ultralong streamer, TransAtlantic Imaging Lithosphere Asthenosphere Boundary (ILAB), which was conducted in spring 2015 (Audhkhazi & Singh, 2019; Marjanović et al., 2015; Singh, 2015). This active-source seismic survey was followed by a passive seismic experiment Pi-LAB (Harmon et al., 2018) recording the earthquake activity within the region focused around and north of the Chain TF for the period of 1 yr (2016–2017). In addition, two active-source seismic refraction surveys were conducted: LITHOS in 2017 (Grevemeyer et al., 2019; Growe et al., 2019; Vaddineni et al., 2019) and ILAB-St. Paul Romanche and Chain (ILAB-SPARC) in 2018 (Gregory et al., 2020; Marjanović et al., 2019). During each of these experiments, interdisciplinary data sets were collected. Below we describe the data sets that are used in this study.

3.1. Bathymetry and Gravity Data

Bathymetry data, shown in Figure 1b, represent a compilation of the high-resolution grids collected during Pi-LAB (Harmon et al., 2018) and high-resolution grids/swaths collected during ILAB-SPARC 2018 (e.g., Marjanović et al., 2019) and LITHOS 2017 (Grevemeyer et al., 2019) expeditions. The total width of the combined swaths is 10–25 km, with a maximum overlap of 5 km (Figure 1c). The data were processed to remove outlier data points and gridded at 50 × 50 m. The bathymetry profile collocated with the seismic line is shown in Figure 2. The detailed characteristics of the bathymetry data collected during the Pi-LAB survey are provided in Harmon et al. (2018) and are not described any further here. To put the bathymetry data into regional context and interpret some of the newly identified features, we use Global Bathymetric Chart of the Ocean (GEBCO) bathymetry data gridded at 15 arc sec (GEBCO Compilation Group, 2019).

The gravity data we use in this study were collected using a Bondenseewerk KSS31 gravimeter during the ILAB-SPARC experiment and are collocated with the seismic lines, both reflection and refraction (Figures 1c and 2). The following corrections were applied to the recorded signal: (1) instrument drift (gravity ties were obtained at the base station located in the port of Mindelo, Cape Verde), (2) latitude correction, and (3) Eötvös correction. To obtain the free-air anomaly (FAA), we subtracted the reference gravity along the GRS80 ellipsoid from the corrected measured signal. We then used the spectral method presented by Parker (1972) to calculate the gravity response for a model that assumes a constant thickness, 6 km thick crust, and the following densities: water 1,035 kg/m³, sediments 1,900 kg/m³ (where present), crust 2,700 kg/m³, and upper mantle 3,300 kg/m³. The calculated signal was subtracted from the FAA to obtain the Mantle Bouguer Anomaly (MBA). The resulting MBA displays the presence of artifacts that are associated with 3-D effect (Figure 2). To eliminate these undesired short-wavelength variations, we calculate a polynomial fit to the MBA profile.

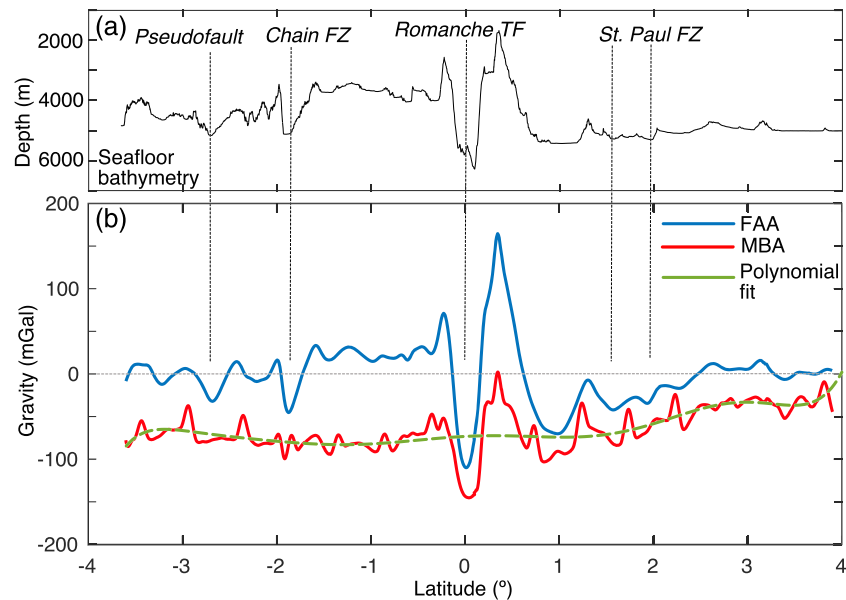


Figure 2. Gravity profile. Panel (a) shows a 2-D bathymetry profile along the line that crosses the Chain and St. Paul FZs, the Romanche TF, and propagator (locations are shown in vertical dotted lines; note that for the St. Paul, we indicate the location of the northern and southern limit of the FZ). In panel (b), we show gravity data collected during the ILAB-SPARC expedition: Free-air anomaly is shown in solid blue line, and calculated Mantle Bouguer Anomaly assuming 6 km thick crust is shown in red with a polynomial fit shown in dashed green line.

3.2. Multichannel Seismic Data

The multichannel seismic (MCS) data were collected during the TransAtlantic ILAB survey in 2015 (Audhkhasi & Singh, 2019; Marjanović et al., 2015; Singh, 2015) and ILAB-SPARC in 2018 (Gregory et al., 2020; Marjanović et al., 2019). During these two surveys, different equipment and acquisition geometry were used for collecting MCS data and are presented separately.

3.2.1. TransAtlantic ILAB MCS Data Set

In spring 2015, high-quality MCS data were collected aboard M/V *Western Trident* that at the time was operated by WesternGeco (Schlumberger). A 12 km long IsoMetrix technology streamer with pressure and three-component accelerometer sensors was used, resulting in 3,840 channels for each component spaced at 3.125 m. The streamer was deployed at 30 m below the sea surface. An airgun array composed of six sub-arrays (deployed at 15 m below sea surface to enhance low frequencies) with eight airguns along each array resulted in a large source volume of 10,170 in³. The shooting interval for the data presented in this work was 62.5 m with record length of 25 s (with 2 ms sampling interval).

A total of 2,775 km of ultra-deep reflection data was acquired along a stair-like 2-D profile (Audhkhasi & Singh, 2019; Mehouchi & Singh, 2018). Here, we focus our analysis and present results for one part of the data (~250 km) collected along the line with a 347° azimuth sampling the region between the Romanche TF and ~Charcot FZ, crossing the Chain FZ and propagator (Figure 1c). The initial processing of the data was done onboard and is outlined in Mehouchi and Singh (2018). An example of a shot gather is shown in Figure 3a. In the postcruise processing steps, we focused on imaging the presence of potential events in the crust and upper mantle. We further conduct data denoising by applying dip filter and boosting low frequencies. The presence of the sediments and igneous basement is shown in Figure 2b. To image the Layer 2A/2B boundary, we explore a range of stacking velocities and source-receiver offsets (e.g., Marjanović et al., 2018). We obtain the best results using 1,900 m/s stacking velocity for source-receiver offsets ranging between 3,000 and 5,500 m (Figure 3c). The analyses of a deeper portion of the MCS data, including the imaging of the Mohorovičić (Moho) discontinuity, are the subject of an ongoing study and will be presented elsewhere. The imaged Layer 2A/2B event is picked and depth converted. For the depth conversion we use a constant velocity of 4,000 m/s (Audhkhasi & Singh, 2019).

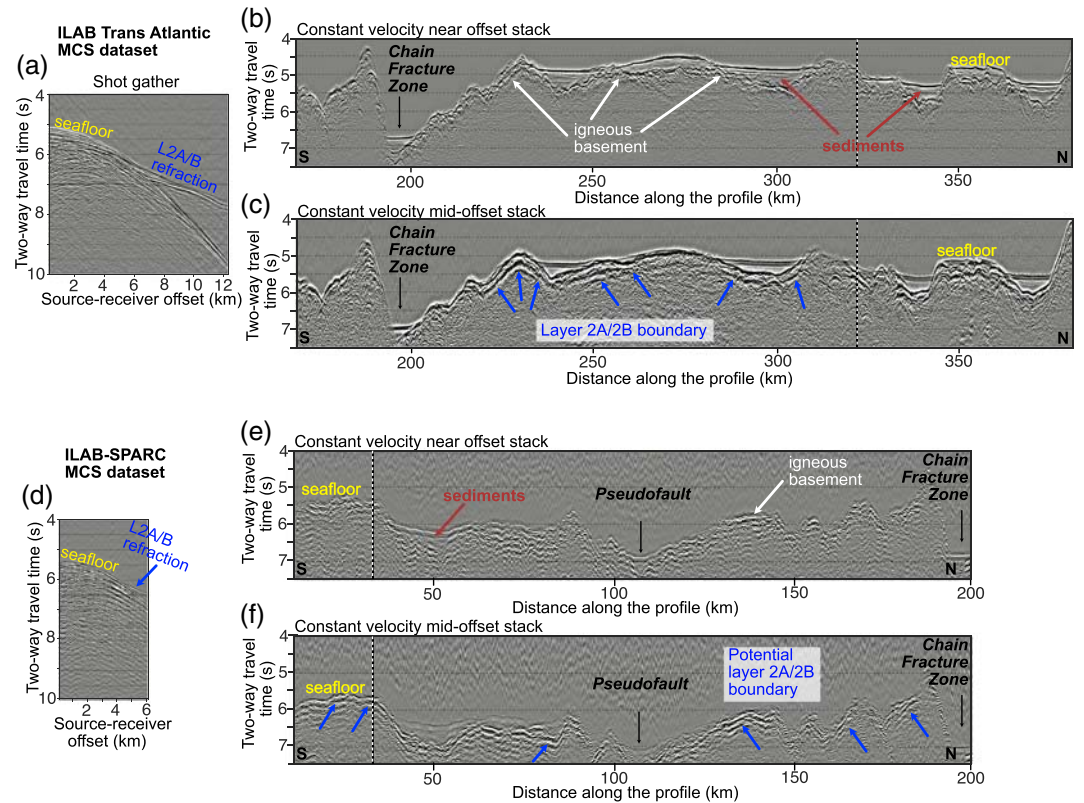


Figure 3. Imaging Layer 2A/2B boundary in seismic data. (top) Processed multichannel seismic (MCS) data collected during TransAtlantic ILAB experiment in 2015: (a) processed shot gather showing ~12 km source-receiver offset; the main upper-crustal events are indicated: seafloor reflection in yellow and Layer 2A/2B refraction branch in blue. (b) Constant water velocity near (<1,500 m) source-receiver offset stack. Note that in this stack, only the presence of sediment pockets (in brown) and the top of the igneous basement (in white) are possible to identify. (c) Constant velocity (1,900 m/s) mid-offset (3,000–5,500 m) stack to show the presence of the Layer 2A/2B boundary indicated in blue arrows. (bottom) Processed MCS data collected during ILAB-SPARC experiment in 2018 (the same color code is used as for the top panels): (d) processed shot gather with ~6 km source-receiver offset. Note that only a small portion of the Layer 2A/2B prograde refraction branch is captured within this data set. (e) Interpolated constant velocity stack for near source-receiver offset stack using the same stacking parameters as in panel (b). (f) An interpolated constant velocity mid-offset stack using the same parameters as for panel (c). Note that the Layer 2A/2B boundary (marked in blue arrows) is present intermittently. In all of the presented stacks, the black-white line indicates the location of the extracted shot gathers shown on the left.

3.2.2. ILAB-SPARC MCS Data

The main focus of the ILAB-SPARC survey, conducted in fall 2018 aboard *N/O Pourquoi Pas?*, was to collect ocean bottom seismometer (OBS) data collocated with the MCS lines acquired in 2015. To assure ideal coverage of the subsurface in OBS data (described in section 3.4), the profile with 347° azimuth was extended both at its northern and southern ends. To sample these regions, during the shooting phase of the ILAB-SPARC survey, a 6 km long streamer with a receiver spacing of 6.25 m was used. The source geometry, volume (4,990 in³), and shot interval (300 m), were designed to fit the OBS data acquisition requirements. The large shot spacing was far from ideal for MCS data collection, but nevertheless, the data are of sufficient quality. An example of a shot gather is shown in Figure 3d. The onboard brute stacks were poststack time migrated using water velocity. These seismic sections were used to pick the seafloor and basement horizons, which were then employed in constraining the velocity profile.

However, to potentially image the Layer 2A/2B boundary, these data needed to be reprocessed. The large shot interval resulted in a low nominal common midpoint (CMP) fold of 10 traces, which is insufficient for Layer 2A/2B imaging. Thus, the first step was to interpolate the data and increase the fold. We interpolate traces in shot domain so that the shot interval is reduced to 75 m, and fold is increased to 40. We also filter the data to include frequencies up to 25 Hz. To further increase the fold to 80, we interpolate traces within

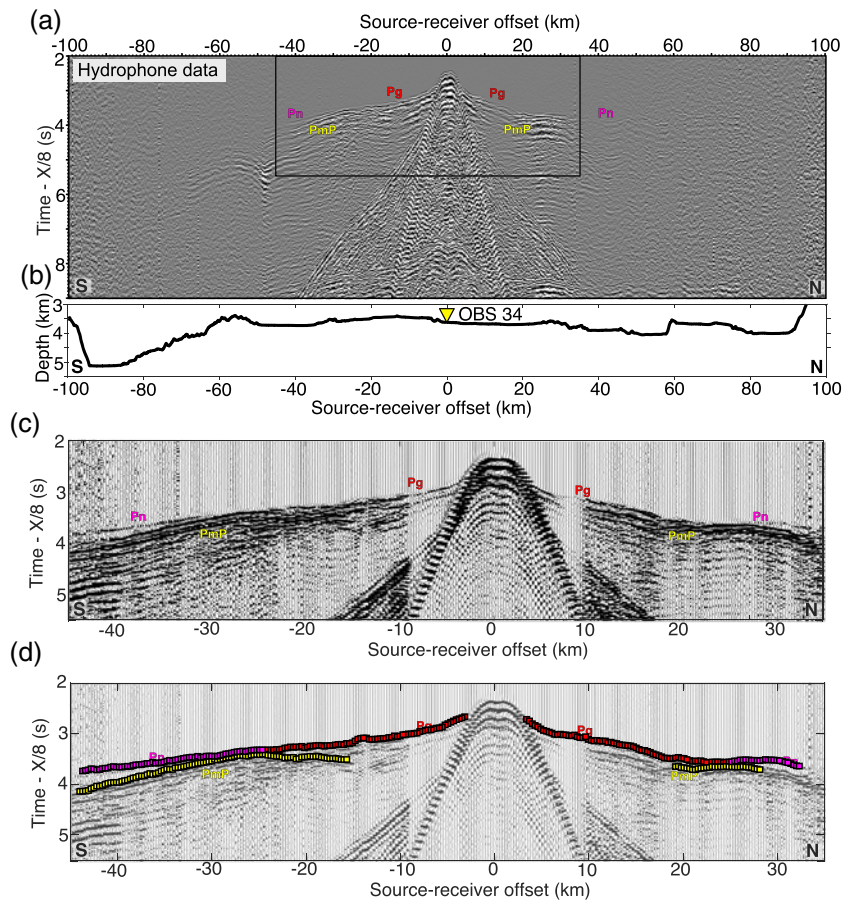


Figure 4. Ocean bottom seismometer (OBS) record. (a) Processed OBS gather recorded on OBS 34 hydrophone component (Figure 1c) displaying 100 km source-receiver offset south and north of the OBS location. The black box encompasses the enlarged region shown in panel (c). The crustal turning ray arrival (P_g) is shown in red, upper mantle turning ray arrival (P_n) is shown in magenta, and wide-angle reflection off the Mohorovičić discontinuity—Moho (P_mP) is shown in yellow. The data shown in the panel were normalized using equal maximum amplitude scaling. (b) Bathymetry profile of the seafloor for the source-receiver range shown in panel (a). The reverse yellow triangle indicates the location of the OBS instrument. In panel (c), we show a wiggle plot of the OBS record within the enlarged region. The markers and color code are the same as in panel (a). (d) The same plot as in panel (c) with a decreased amplitude scale for better visibility of the picked arrivals. The squares show the locations of the actual picks using the same color code as in panel (a).

each CMP gather. To produce a stack that favors imaging the Layer 2A/2B boundary, we use the same stacking velocity as for the MCS data collected in 2015 (section 3.2.1). However, due to the greater depth of a ~ 24 Macrust imaged by our seismic line, the optimal source-receiver offset range was from 4,500–5,000 m. For depth conversion of the event picked in two-way travel time (TWTT), we use the same velocity as for the MCS section sampling the region north of the Chain FZ. The final seismic stacks are shown in Figures 3e and 3f.

3.3. OBS Data

The data were collected using four-component MicroOBS instruments (Auffret et al., 2004), recording data at a sampling frequency of 250 Hz. Prior to converting the OBS record to SEG-Y format, the correction for the internal clock drift was done. Along the profile, 50 instruments were deployed recording seismic source signal produced at every 300 m using a $4,990 \text{ in}^3$ tuned air gun array, towed at 10 m below sea surface. Here, we analyze the data recorded on 25 OBSs (from Numbers 26 to 50, as shown in Figure 1c) located south of the Romanche TF at an approximately equidistant interval of 14.2 km. The exception is the distance between Instruments 39 and 40 within the Chain FZ: These two instruments were deployed slightly farther apart to assure good coupling with the seafloor within the FZ. The OBSs were relocated (Creager & Dorman, 1982)

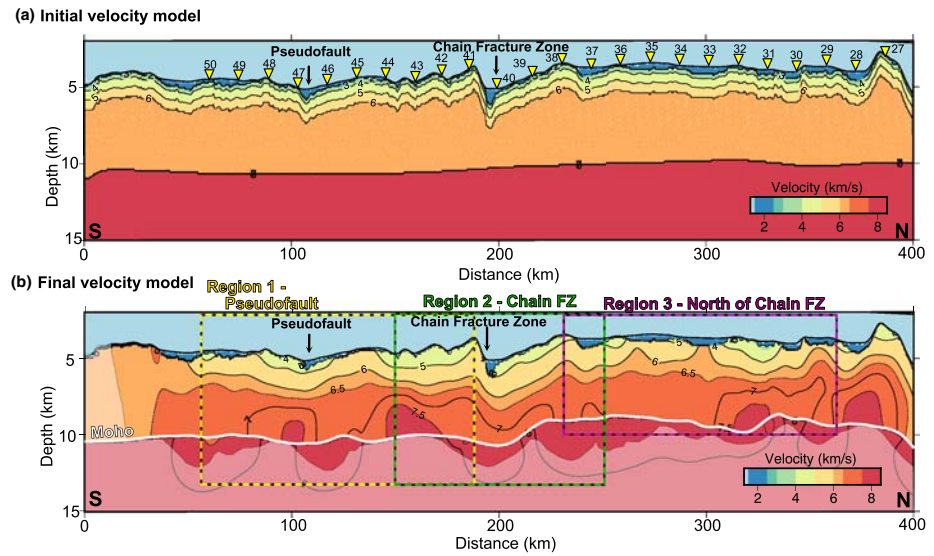


Figure 5. Velocity models. (a) Two-dimensional starting velocity model obtained by extrapolating 1-D velocity function from White et al. (1992). The inverted yellow triangles indicate the location of OBS instruments, which are numbered. (b) Two-dimensional final velocity model obtained using ray-based travel time tomography (Van Avendonk et al., 1998, 2004) to invert for crustal and mantle turning ray arrivals (Pg and Pn, respectively) and Moho reflection (PmP). In white line, we indicate the presence of seismically inferred Moho. The three colored boxes outline the regions around the pseudofault (yellow), the Chain FZ (green), and the zone extending north of the Chain FZ (purple). These three regions are shown in Figure 9. The white transparent zone in panel (b) marks the region outside of the ray coverage.

using the least squares method: The search was conducted within 500 m horizontal and 300 m vertical radius based on minimization of the misfit between the observed and calculated direct water wave picks within 10 km source-receiver offset. The water velocity function was defined using the combination of water-column sound speed from onboard expendable bathythermograph (XBT) measurements and legacy World Ocean Circulation Experiment (WOCE) conductivity-temperature-depth (CTD) data.

For analyzing the arrivals, we use the data recorded on the hydrophone component, to which we apply a minimum-phase band-pass filter with the frequency range of 3–24 Hz (Figure 4a and supporting information Figures S1, S2a, and S3a). A predictive deconvolution was applied to the data for plotting purposes only. We identify turning rays in the crust (Pg), turning rays in the upper mantle (Pn), and wide-angle reflection off Moho (PmP). The Pg arrivals are identified within source-receiver offsets up to ~30 km (Figures 4, S2, and S3). The total number of manually picked Pg arrivals for our 25 OBSs is 3,843. The Pn arrivals are normally identified within offsets ranging between ~30 and ~60 km with a total number of picks of 2,760. The PmP arrivals are identified in all of the OBS records included in this study, with a total number of picks of 2,159. For each set of the picks, we define picking error based on the clarity of the signal. Most of Pg arrivals were clear with the picking error varying between 30 and 50 ms. The reflection signal from Moho in some instances was overprinted by a bubble pulse and/or noise, which resulted in higher picking error. Overall the picking error for PmP arrivals varied from 30 to 80 ms. Due to lower signal-to-noise (S/N) ratio at farther source-receiver offsets, the picking error for Pn arrivals varied widely from 30 up to 150 ms. Although we could follow the first arrivals up to 700 km source-receiver offset in a number of OBS records (e.g., Marjanović et al., 2019), here, we limit the analysis of the arrivals to source-receiver offsets <100 km as we focus mainly on the crustal characteristics. The arrivals identified at larger source-receiver offsets will be addressed elsewhere.

3.4. Ray-Based Travel Time Tomography

We base our analyses on the joint inversion of all the observed arrivals, that is, Pg, PmP, and Pn using the method developed by Van Avendonk et al. (1998, 2004). Within this approach, the ray-tracing algorithm, which solves the forward problem, uses the shortest-path modeling to obtain a global minimum of predicted travel times and trace the rays between sources and receiver for a given velocity model. In addition to

modeling refraction arrivals, the algorithm is designed to model reflection arrivals by forcing raypaths to reflect from a predefined interface point, in our case points along a crust-mantle boundary or Moho. As a starting velocity model, we use a simplified 1-D velocity function, which is based on White et al. (1992) and Grevemeyer et al. (2018), and extend it to 2-D (Figure 5a). The modification is reflected in the velocity of the sediments that we obtain as an average velocity from conducted semblance velocity analyses of the MCS data in the given region, which is 1.86 km/s. In the starting velocity model, we assume that the Moho is represented by a smooth surface at ~6 km below the igneous basement. Thus, our initial crustal thickness was roughly 1 km thinner when compared to the Atlantic crust as defined by White et al. (1992), using an average crustal thickness as defined by Chen (1992). Our inversion procedure focused therefore on defining deviations of crustal structure from normal oceanic crust. The grid spacing of the starting model is 200 m horizontally and 50 m vertically. We extend the length of the original shooting line by 6 km on each side to avoid potential edge effects.

The inversion algorithm uses a least squares approach to minimize the difference between the calculated travel times obtained as a solution of the forward problem and the travel times of the manually picked arrivals (details behind the algorithm itself are provided by Van Avendonk et al., 2004). The perturbation model at each iteration is defined on a grid with 400 m horizontal and 100 m vertical grid spacing. At each iteration, we apply a set of smoothing parameters that control the lateral smoothing of the velocity grid, velocity jumps, and smoothness of the Moho interface. In the first step, we invert Pg arrivals only. Once we obtain a satisfactory velocity model of the crust, we invert Pg and PmP, which, in addition to the velocity model, provides the constraints on the Moho depth. Finally, using the resulting model, we invert for all of the examined arrivals, that is, Pg, PmP, and Pn (Figure 5b), in order to determine the upper mantle velocity just below the Moho.

As a way to quantify the data fit, we use a standard χ^2 value (e.g., Van Avendonk et al., 1998). At each iteration, we set a target value for χ^2 ; the χ^2 values follow an exponential trend, that is, decrease rapidly for the first several iterations to reach the targeted value $\chi^2 = 2$ at the final iteration. Together with the χ^2 , we also adjusted parameters that control magnitude of the velocity model update, smoothness of the model, and flatness of the Moho reflector. Typically, greater smoothing/flatness constraints were applied during the first iterations to keep the inversion stable. They are also higher in the first step of the inversion when inverting only for crustal turning ray arrivals (i.e., Pg). Examples of raypaths through the final velocity model and travel time residuals are given in Figures S4 and S5. The resolution power of the model is examined using derivative weight sum (DWS) (Toomey & Foulger, 1989) and checkerboard test (Figures S6 and S7, respectively). The model has good ray coverage between 50 and 350 km distance range along the profile, and checkerboard test results can resolve 5% magnitude anomalies of a minimum size of ~20 km. In addition, we examine uncertainty in the velocity model and depth of Moho (Figures S8 and S9). The former test results show that throughout most of the model, the uncertainty in the resolved velocity is <0.1 km/s (Figure S8). The highest uncertainty is observed at ~350 km along profile distance, where we have low ray coverage (Figure S6). For examining uncertainties in the Moho depth, we follow the approach of Canales et al. (2003) and introduce sinusoidal perturbations to the Moho surface (Figure S9). The test shows that we can detect variations in the Moho depth ≥ 700 m.

4. Results

4.1. Observations in Bathymetry and Gravity Data

We describe the observations from recently collected gravity and high-resolution bathymetry data and put them into a regional context using global bathymetry (GEBCO) and gravity data sets and results from previous studies (Bonatti et al., 1991, 1994, 2001; Bonatti, Ligi, Carrara, et al., 1996; Harmon et al., 2018).

4.1.1. Ridge Segment Between the Chain and Romanche TFs

A first-order tectonic segment of the MAR that is delimited by the Chain and Romanche TFs displays a complex ridge axis morphology (Figure 1b). The bathymetry characteristics of its southern portion were mapped in detail during the Pi-LAB experiment (Harmon et al., 2018). The results suggest that the region directly north of the Chain TF is characterized by a magmatically starved segment end. However, past this relatively narrow zone, to about the center of the segment, the ridge axis extends almost linearly with well-developed abyssal hills suggesting a more magmatically robust part of the segment. Although we do not have high-

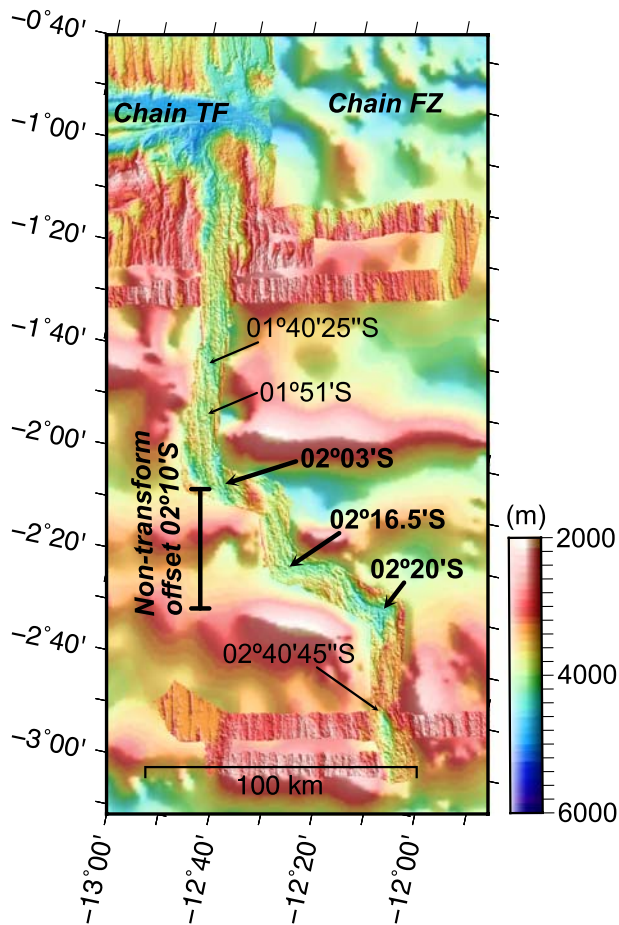


Figure 6. Bathymetry map of the first-order tectonic segment extending south of the Chain TF. The background is represented by GEBCO data on which high-resolution bathymetry data collected during the LITHOS experiment (Grevemeyer et al., 2019) are superimposed. The arrows indicate higher-order (second- and potentially third-order) discontinuities we identified in the seafloor.

resolution bathymetry available for the northern half of this segment, we can identify from the global bathymetry data grid (Figure 1b) a change in ridge axis character at $\sim 00^{\circ}43.5'S$. At this point, the axial valley narrows and shallows. Another change in the axial valley, similar in nature, is observed at $\sim 00^{\circ}20'S$. Following the nomenclature introduced by Macdonald et al. (1988), these two locations could be defined as NTO discontinuities that delimit an ~ 40 km long second-order ridge segment. Further to the north of this segment, the ridge axis bends toward the Romanche TF (e.g., Bonatti, Ligi, Carrara, et al., 1996; Bonatti et al., 2001). This obliquely trending ridge section is also characterized by several higher-order tectonic segments (at least six) that are 25–30 km long. The exact locations of these discontinuities are not possible to identify as for this region we only have a compilation of low-resolution bathymetry data sets available.

Along the bathymetry swath, which follows the OBS line and samples ~ 7 – 10 Ma old lithosphere, we can identify two distinct zones (Figure 1c), a southern zone and a northern zone. From the Chain FZ to about the middle part of the segment (\sim OBS 33; Figure 1c), we observe two well-developed linear seafloor features (40–50 km long and separated by 5 km) with ridge-parallel orientation. We interpret them as sediment-buried abyssal hills that were formed during a more magmatically robust phase of the southern portion of the MAR segment ~ 10 Ma ago. Their spatial extent corresponds to the more magmatically robust, southern part of the present-day ridge axis (Figure 1b). North of this region, the seafloor in the bathymetry data swath is characterized by rough bathymetry and an absence of oceanic spreading fabric.

4.1.2. Ridge Segment Between the Chain and Charcot TFs

A first-order tectonic segment between the Chain and Charcot TFs extends for ~ 240 km (Figure 6). It is interrupted by a zone of three second-order, step-sided tectonic discontinuities, that is, NTOs (e.g., Carbotte et al., 2015; Sempéré et al., 1993). We define this highly segmented portion of the ridge axis as an NTO discontinuity region,

centered at $02^{\circ}10'S$ (hereinafter, the $02^{\circ}10'S$ NTO Zone). In fact, the contemporary morphology of the $02^{\circ}10'S$ NTO Zone is rather complex. It is represented by a ~ 50 km along-axis zone extending between $02^{\circ}03'S$ and $02^{\circ}20'S$, encompassing three right-lateral discontinuities (Figure 6): the northern at $\sim 02^{\circ}03'S$ offsetting the ridge axis by ~ 30 km, the central at $02^{\circ}16'S$ with 25 km offset, and the southern one at $02^{\circ}20'S$ with ~ 15 km offset. The ridge segment delimited by the northern and central discontinuity within the $02^{\circ}10'S$ NTO Zone is ~ 35 km long.

The northern second-order segment, extending between the Chain TF and $02^{\circ}10'S$ NTO Zone (~ 120 km long), is represented by relatively linear abyssal hills, which may suggest a magmatically more robust segment. Its northernmost part, about the first 30 km south of the Chain TF, displays deep topography and the presence of core complex structures on the western flank (Harmon et al., 2018), which argues for the presence of a magmatically starved segment end. Along its extent, using the available bathymetry data, we could identify a couple of higher-order discontinuities (Macdonald et al., 1991) at $01^{\circ}40'25''S$ and $01^{\circ}51'S$.

The ridge segment extending between the $02^{\circ}10'S$ NTO Zone and Charcot TF display two distinct parts (Figure 6), the northern part with a relatively shallow ridge axis (the shallowest point is $\sim 3,100$ m) and the southern part represented by a relatively deep axial valley ($>3,800$ m on average). The change in depth between these two parts is identified at $02^{\circ}40'45''S$ with an abrupt step of ~ 880 m. This significant difference in depth of the ridge axis could suggest that these two segments are in two different phases of ridge spreading, northern, in magmatic, and southern, in tectonic ridge spreading phase.

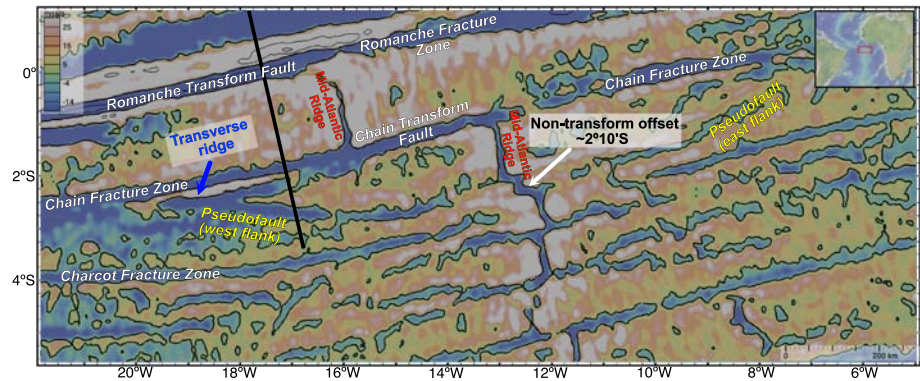


Figure 7. Global free-air anomaly map (Sandwell et al., 2014) for the equatorial Atlantic region with the interpretation of the main tectonic features indicated. The black line shows the location of the OBS line collected during the ILAB-SPARC cruise. The map is made using GeoMapApp (Ryan et al., 2009).

4.1.3. Pseudofault

A pair of obliquely trending linear structures, which we identify as pseudofaults (Hey et al., 1980; Kleinrock & Hey, 1989), is evident in the global gravity (Figure 7; Sandwell et al., 2014) and global bathymetry data (Figure 8). We suggest that this typical “V”-shape feature is a result of a southward propagation of a second-order MAR segment located south of the Chain TF.

On the west flank of the MAR axis, we observe the onset of the pseudofault at the intersection with the Chain FZ within ~46 Ma old lithosphere, which coincides with an important change in relative plate motion between the South American and African Plates (Müller et al., 1999) that also dominated the deformation

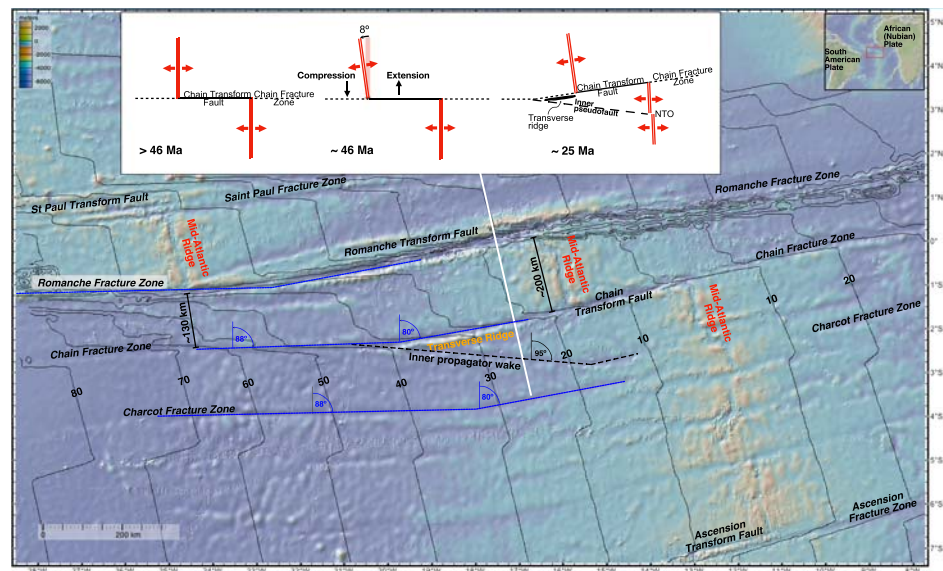


Figure 8. Global bathymetry map of the equatorial Atlantic region. The main morphotectonic features represented by the Mid-Atlantic Ridge and transform discontinuities (transform fault and fracture zone domains) are marked. The white line indicates the location of the seismic refraction profile. Blue dotted line indicates the general trend of the Chain Fracture Zone on the western flank to emphasize the change in plate kinematics that happened between 46 and 38 Ma. In blue dotted lines we mark the general trend of the Romanche and Charcot FZs, which also display the prominent change of 8°. Black dashed line outlines the pseudofault on the west flank of the ridge axis and its transition to the off-axis track of the NTO 02°10'S. The lithospheric ages (Müller et al., 2008), as well as the background bathymetry map, are from GeoMapApp (Ryan et al., 2009). In the inset, following Bonatti (1978), we indicate the possible change in near-field stresses that could potentially explain the formation of the transverse ridge we observe on the southern wall of the Chain FZ.

history of the St. Paul transform discontinuity system (Maia, 2018). From the intersection with the Chain FZ, the pseudofault extends continuously farther to the south in a $\sim 95^\circ$ azimuth. At ~ 17 Ma, it intersects with an almost ridge-perpendicular off-axis trace of the $02^\circ 10'S$ NTO Zone. This intersection indicates the cessation of the southward propagation of the ridge tip at the NTO discontinuity. On the east flank of the MAR axis, the trace of the propagator's tip is more subdued and fragmented (Figure 7). Our profiles, both OBS and MCS, cross only the pseudofault on the west flank ~ 80 km south of the Chain FZ (Figure 1b). In the MCS data, it is identified as a ~ 8 – 10 km wide trough (~ 400 m difference in depth), filled with 500 m of sediments (Figure 3f).

It is interesting to note that the portion of the MAR extending between the right-lateral Chain TF and left-lateral Ascension TF is characterized by several discontinuities that offset the ridge axis by less than 50 km (Figure 8). One of these smaller-offset discontinuities is the long-lived Charcot FZ, the trace of which for the past 10–14 Myr exhibits significant complexities.

4.1.4. Transverse Ridge

Along the southern wall of the Chain FZ, representing the older lithospheric block, we observe a prominent feature that we identify as a transverse ridge. The feature extends continuously for about 320 km starting from 120 km west from the western RTI (Figure 1b). Its signature is also prominent in the global gravity data (Figure 7). Along most of the strike of the transverse ridge, the seafloor depth varies from 2,000 to 3,000 m. However, the westernmost tip of the transverse ridge deepens almost abruptly to 4,000 m as it approaches the intersection between the Chain FZ and the pseudofault.

4.1.5. Gravity Data

Along most of the length of the sampled 2-D gravity profile, the FAA signal mimics the seafloor bathymetry (Figure 2). The exception to the above is the region north of the St. Paul FZ, where the gravity anomaly is stronger, although no evident change in bathymetry is present across this FZ. South of the Romanche TF, the biggest changes in the FAA are observed across the Chain FZ and the pseudofault, of 80 and 48 mGal, respectively. Across the Chain FZ, the region north of the fracture has, on average, ~ 30 mGal higher FAA. In addition, for this region, we also see a decrease of 15 mGal in calculated (average) MBA (assuming 6 km thick crust).

4.2. Layer 2A

The Layer 2A/2B boundary is imaged along $\sim 38\%$ of the OBS line (Figure 3). However, as we use constraints from two MCS data sets of different quality (section 3.2), we will present separately the results obtained using each data set.

Along the portion of the line that samples the region between the Chain FZ and Romanche TF using the long-streamer 2015 MCS data, we can clearly distinguish two zones (Figure 3c). The first zone extends north of the Chain FZ to about midway of this first-order tectonic segment (between 200 and 305 km along the profile distance [apd]). It is characterized by an intermittent but high-amplitude signal of the Layer 2A/2B boundary imaged at an average 550 ± 35 ms TWTT beneath the igneous basement (or $\sim 1,100$ m thickness). The brightest and most continuous portion of this topmost crustal boundary is imaged immediately north of the Chain FZ, from 220 to 260 km apd. In its southern part, it deepens from ~ 390 m below the seafloor peak (at ~ 230 km apd) to $\sim 2,000$ m as it approaches the northern wall of the Chain FZ, where it disappears. We need to mention that the latter depth estimate may be associated with a larger picking error as the northern wall of the FZ exhibits topographic short-wavelength variations, which increase the uncertainty in our picks of the seafloor as well as the Layer 2A/2B boundary. North of this region, right beneath the dome-shaped feature observed in the bathymetry (between 260 and 285 km apd), we cannot identify the presence of signals originating from the Layer 2A/2B boundary. The seafloor within this region is relatively flat and partially covered by a thin layer of sediments, which can be characterized as almost ideal conditions for imaging the base of Layer 2A, if present. The reason why we do not observe the signal from the Layer 2A/2B boundary is most probably geological. North of this subregion, we identify an ~ 25 km wide basin filled up with sediments. Beneath this basin, the signal from Layer 2A/2B boundary is present but very complex, with a gap in its middle part. The presence of the gap becomes much clearer in the velocity model (Figure 5b). In contrast, the portion of the profile extending between the segment center (at ~ 305 km apd) and the southern wall of the Romanche TF is characterized by rough seafloor topography and the absence of the Layer 2A/2B boundary.

Although the ILAB-SPARC MCS data that sample the region south of the Chain FZ (including the pseudofault) have a lower resolution, we can observe the Layer 2A/2B boundary intermittently along ~40% of the profile extent (Figure 3f). It needs to be mentioned that for the parts of the profile with considerable seafloor depth (>5 km), as is the case for the region between 90 and 120 km apd, the Layer 2A/2B boundary may not be observed not only due to geology but also due to our inability to capture the signal with the 6 km long streamer. The shot gather in Figure 3d shows that for the shallower parts (~4 km), the Layer 2A/2B signal is observed at offsets greater than 4.5 km. For the portions of the profile that display the presence of the event that we interpret as a Layer 2A/2B boundary, we find that the thickness of Layer 2A varies between 720 and 3,040 m, with an average value of ~1,880 m. However, due to both the interpolation we applied to compensate for the large shot intervals and the possible picking error (varying between ± 50 and ± 75 ms), the above values should not be regarded as absolute thicknesses of the topmost crustal layer within the area but rather as approximate values.

4.3. Crustal and Upper Mantle Properties From the Velocity Model

The preferred velocity model (Figure 5b), obtained using the wide-angle seismic refraction data, spans ~350 km of oceanic lithosphere and shows that overall crustal velocities are higher than proposed in the initial model. The average igneous crustal thickness is 5.4 km, which is lower than the reference crustal thickness of 6–6.2 km as defined by the passive upwelling model (Forsyth, 1993) and a global compilation (Chen, 1992; Christeson et al., 2019) and much less thinner than the thickness of 7.1 km reported by White et al. (1992) for the crust formed at the MAR. As the profile crosses two distinct features from morphotectonic point of view, the Chain FZ and the pseudofault (Figure 5b), we divide the profile into three regions and present the results for each region separately.

Region 1—Pseudofault

Along the profile, we define the pseudofault to extend between ~90 and 140 km distance along the profile (Figures 5b and 9a), based on the bathymetric expression (Figure 10a). Within this ~50 km wide pseudofault zone, we observe prominent changes in the thickness of the igneous crust from (1) its southern portion, which shows ~5.7 km thick igneous crust, to (2) 0.7 km thinner crust within the central part, followed by (3) gradually thickening of the crust toward the north where the maximum thickness of ~6.2 km is observed (Figure 10b). Furthermore, upper-crustal to midcrustal velocity values (first 3 km of the crust) display almost the opposite pattern: While lower velocity (~5–5.2 km/s) is observed in the southernmost part, higher velocity (~5.5–5.7 km/s) is present over the central and northern parts of the pseudofault (Figure 10c). Note that this part of the crust, termed here upper crust to midcrust, represents the zone that is densely sampled by the crustal Pg arrivals (Figure S6). Although the velocity values obtained from the lower portion of the crust are not well constrained by the propagated rays, the average velocity function, calculated within a 2 km wide horizontal band above the Moho, does not mimic the crustal thickness variation pattern observed within the pseudofault. This observation suggests that the resulting thickness variations are real and do not represent a trade-off of crustal velocity variation and crustal thickness. For the younger and older crust side, juxtaposed north and south to the pseudofault, respectively, we observe a similar crustal thickness, ~5.4 km on average. It is interesting to note that from south to north (younger-to-older crust) across the pseudofault, the lower crustal velocities sharply decrease, whereas upper-crustal velocities increase (Figure 9a).

Region 2—The Chain FZ

We define the Chain FZ region to extend between the bathymetric peak of the southern wall (top of the transverse ridge) and about the middle of the gently steeping northern wall, that is, between ~190 and 215 km apd (Figures 5b and 9b). The latter boundary is coincident with the limit of the Layer 2A/2B boundary observations. Within this region, we observe on average ~5.4 km thick crust (Figure 9b). However, a very localized thin crust (~4.6 km) is observed directly beneath the narrow (~10 km wide) sedimentary basin, which forms the welded contact between the older (southern) and younger (northern) lithosphere on both sides of the FZ. The thickest crust is observed right below the transverse ridge, ~6.3 km. Within the 30 km wide zones of older and younger crust to the south and north of the FZ, respectively, we observe different thicknesses: ~5.9 km to the south (or 5.7 km when we exclude the region directly below the transverse ridge) and ~5.2 km to the north. In terms of upper-crustal velocity, if we exclude the region directly beneath the transverse ridge, velocities beneath the FZ valley and beneath the older crust side are similar, that is, ~5.2 km/s. However, on the younger crust side within the 30 km wide zone north of the Chain FZ, we do

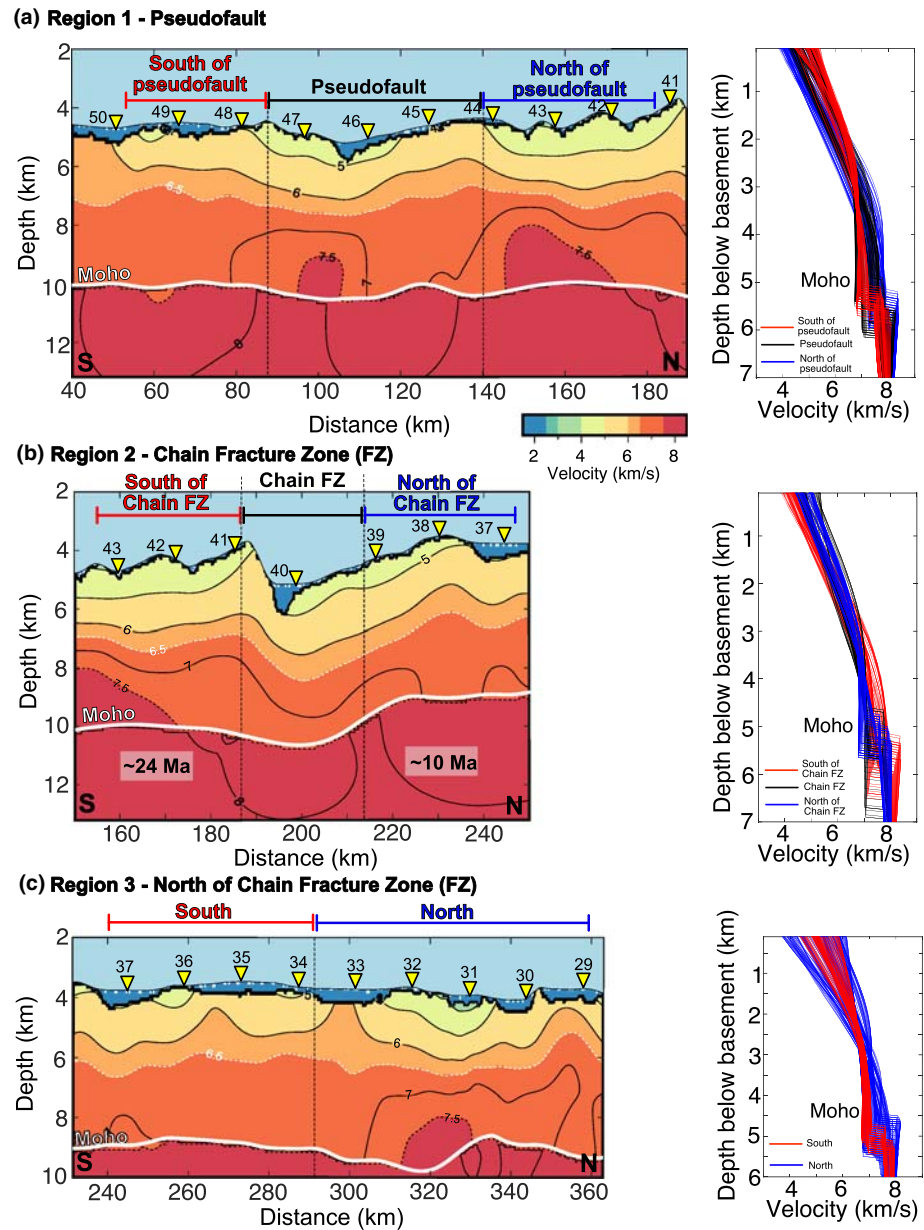


Figure 9. Close-up velocity models for (a) Region 1—the pseudofault, (b) Region 2—the Chain Fracture Zone, and (c) Region 3—the zone north of the Chain FZ. The location of each of the regions is shown in the 2-D profile in Figure 5b. Within each panel we identify zones from which we extract 1-D velocity functions spaced at 800 m for comparison. The extracted 1-D velocity functions are shown in the right of the corresponding region. The remaining elements are the same as in Figure 5.

observe a gradual velocity increase of ~ 0.4 km/s. The lower crustal velocities, although not well constrained by our model, are relatively uniform at ~ 7 km/s but with large standard deviations (Figure 10d).

Region 3—North of the Chain FZ

This part of the model extends between 240 and 360 km apd, and samples 7–10 Ma old crust (Müller et al., 2008) formed along a first-order tectonic MAR segment (Figures 5b and 9c). We limit the extent of the northern end of the examined zone to eliminate any possible effect of the Romanche TF (Gregory et al., 2020). Within this region, based on the crustal thickness and velocity characteristics, we can clearly identify two subregions: the southern one extending from the Chain FZ to about the middle of the segment (i.e., between 240 and ~ 290 km apd) and the northern one that extends between the middle of the segment

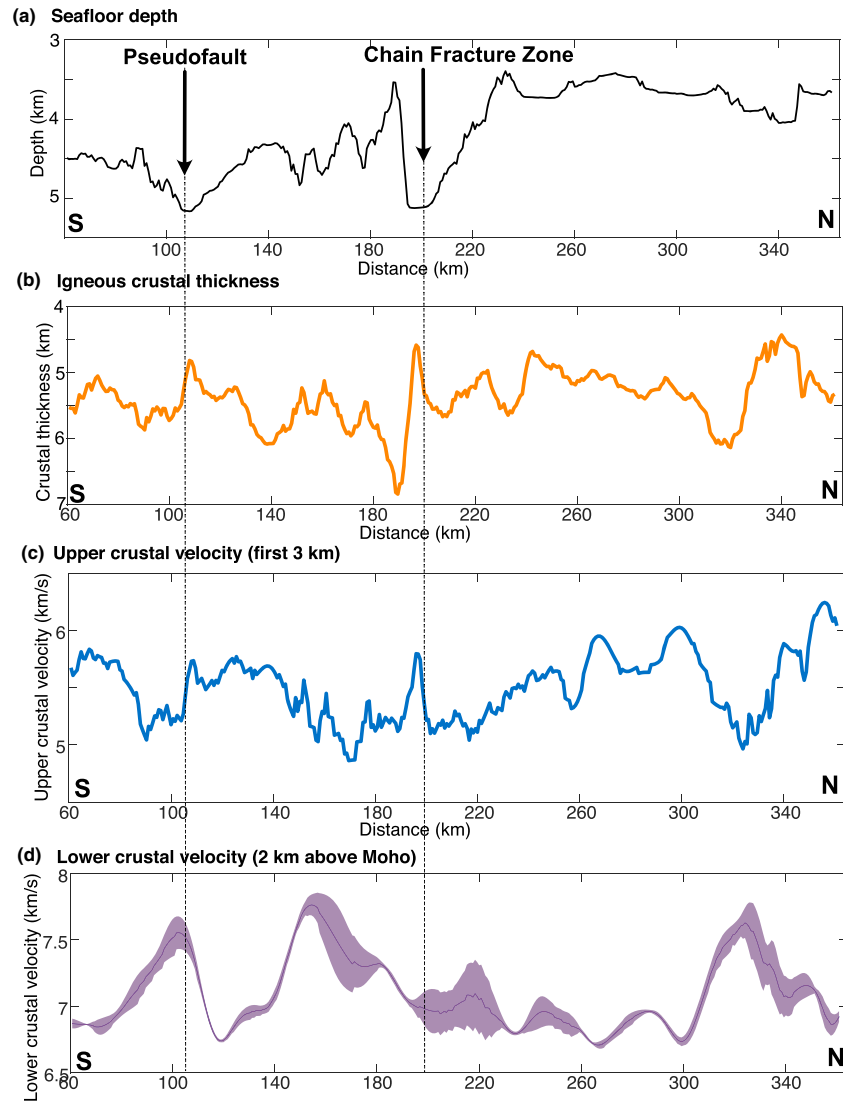


Figure 10. Parameters depicting crustal structure along the examined 2-D line: (a) seafloor depth; (b) igneous crustal thickness; (c) average velocity for the upper 3 km of the oceanic crust; and (d) average 1-D velocity profile (thin purple line) for 2 km of the lower oceanic crust above the Moho. The shaded purple region represents the limits of standard deviation.

and south of the Romanche TF (i.e., between 290 and 360 km apd). The southern part displays thinner oceanic crust, on average ~ 5.1 km. Velocities within the upper igneous crust (<3 km) are relatively uniform, with the exception of the region beneath the dome-shaped structure where an increase in velocity function is observed. This is also the zone in which we do not observe the presence of Layer 2A/2B boundary in the seismic section (section 4.3). The lower part of the crust does not display any complexities and is almost constant throughout this subzone. In contrast to the southern subzone, the northern subzone shows important variability, both in terms of crustal thickness and the velocities. A wide range of thicknesses is observed: from 6.3 km, between 310 and 320 km along profile distance, to 4.4 km as we approach the Romanche TF. In addition to the large variation in crustal thickness, the upper-crustal to midcrustal velocity also varies significantly (Figure 9c), with a minimum value of 5.2 km/s identified at the transition from very thick crust in the south to thin crust in the north (~ 320 km apd). Interestingly, the lowest velocity within the upper 3 km of the crust (5 km/s) coincides with the highest lower crustal velocity 7.6 km/s. As upper-crustal velocities are constrained by Pg arrivals and the lower crustal velocities from PmP, these differences are most probably real. However, we need to mention that the crustal

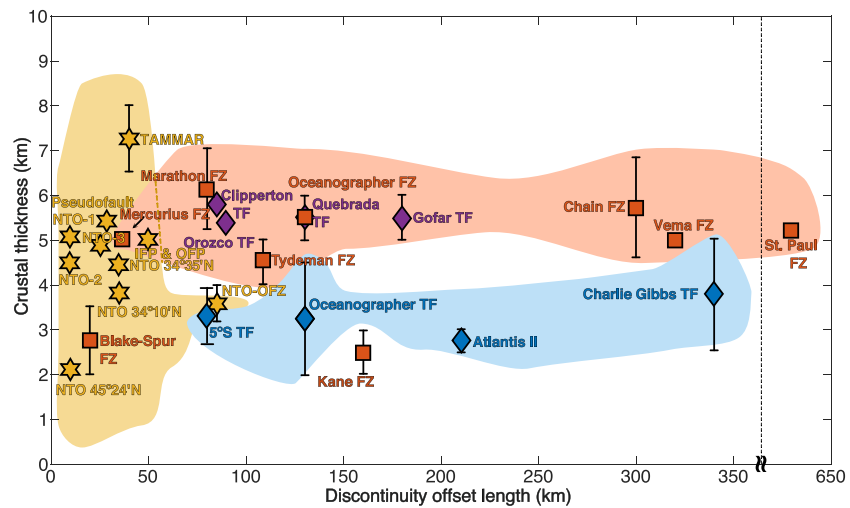


Figure 11. A summary plot of crustal thicknesses derived from seismic data across a number of fracture zones (orange square), transform faults (blue diamond), and nontransform offsets (yellow star) versus discontinuity offset length (see text for the references). For the cases where the range of crustal thickness was reported, the range is indicated by error bars and the average crustal thickness is indicated in the corresponding symbol. The vertical dashed line indicates interruption in horizontal axis to show the crustal thickness for the St. Paul FZ (Grove et al., 2019) displaying a cumulative offset of 630 km (e.g., Maia et al., 2016). The IFP and OFP stand for inner and outer pseudofaults, respectively, from Dannowski et al. (2018). The color shaded zones are used only as eye guides.

thickness/velocities for the northern subzone may not be as well constrained as for the southern subzone, and the results should be taken rather as a relative variation with respect to the initial velocity model.

5. Discussion

5.1. Crustal Thickness Across the FZs and NTOs

During the 1980–1990s a number of active refraction studies were conducted examining transform discontinuities offsetting the MAR: Kane (Cormier et al., 1984; Detrick & Purdy, 1980), Vema (Detrick et al., 1982; Potts, White, et al., 1986), Blake Spur (Minshull et al., 1991; Mutter et al., 1984; White et al., 1990), Oceanographer (Ambos & Hussong, 1986; Fox et al., 1976; Sinha & Loudon, 1983), Charlie Gibbs (Whitmarsh & Calvert, 1986), and Tydeman (Calvert & Potts, 1985; Potts, Calvert, et al., 1986). A large majority of these studies used the active sources and a limited number of ocean bottom hydrophones (OBHs) and/or OBSs. The exceptions are the studies conducted at the Vema FZ (Ludwig & Rabinowitz, 1980) where sonobuoys were used and at the Blake Spur FZ (Minshull et al., 1991; Mutter et al., 1984) where the results were based on the interpretations of MCS and expanding spread profiles (ESP) data sets. In addition to the studies at the MAR, using eight OBH instruments, Muller et al. (2000) examined crustal structure across TFs at 57°E and 66°E offsetting the slow-spreading Southwest Indian Ridge. More recently, a modern OBS survey using 54 instruments along a 225 km long seismic line was carried out across the Marathon FZ and three NTOs (NTO-1, NTO-2, and NTO-3) over a ~65 Ma central Atlantic lithosphere (Davy et al., 2020). This recent results for the Marathon FZ are falling within the crustal thickness range from 5.2 to 7 km reported by Peirce et al. (2019) for the same FZ examined closer to the ridge axis (~1 Ma crust). In addition, Peirce et al. (2019) also examined the crustal structure beneath the Mercurius FZ where ~5 km thick crust is inferred. The resulting range of crustal thicknesses and compressional seismic velocities obtained by the earlier studies conducted along the MAR was quite wide, varying from as thin as 1 km to as thick as the average crustal thickness value of >6 km observed at slow-spreading ridge segments.

By examining the results of these earlier active-source seismic studies focused on transform discontinuities, we realized that one of the reasons for the observed wide-range variations in crustal thicknesses and/or crustal velocities is due to a nonunique terminology. In most of the seismic studies during the 1980s, the whole transform discontinuity system was collectively termed as “fracture zone”, that is, there was no clear

distinction between the TF and FZ domains. Based on the location of the seismic profiles presented in the literature, we made a compilation separating the results obtained for the FZ and TF domains. In Figure 11, we show the resulting crustal thicknesses mapped at different TFs and FZs (including this study, i.e., the Chain FZ, and the preliminary result for the St. Paul FZ reported by Growe et al., 2019) offsetting slow-spreading centers. Also, we add crustal thickness detected at a number of NTOs (Canales et al., 2000; Dannowski et al., 2018; Davy et al., 2020; Detrick et al., 1993; Dunn et al., 2017; Hooft et al., 2000; Kahle et al., 2016) to enable potential comparison with the crustal thickness obtained across the pseudofault formed by the ridge propagation. For completeness, we include estimates from fast-spreading centers, where results are only available for the TF domains (e.g., Roland et al., 2012; Tréhu & Purdy, 1984; Van Avendonk et al., 1998).

Overall, our compilation, representing the variations in crustal thickness (for slow-slipping transforms) as a function of transform offset length, outlines two distinct regions (Figure 11). The first cluster is observed for lower crustal thicknesses (<4 km; blue zone in Figure 11) and includes predominantly crustal thickness values obtained for different TF domains at slow-spreading centers (i.e., Oceanographer, Charlie Gibbs, and Atlantis II). Note that the crustal thickness mapped within the TFs at fast-spreading centers (Clipperton, Orozco, Quebrada, and Gofar) is >2 km higher. The second cluster, which spans offset lengths larger than 50 km (orange zone in Figure 11), displays crustal thicknesses greater than 4 km and encompasses the results obtained from seismic studies on FZs of different transform discontinuity systems at slow-spreading centers. The crustal thickness we detect across the Chain FZ falls well within the latter cluster, confirming the pattern. Exceptions to this trend are the Kane and Blake Spur FZs, which display significantly thinner crust (Cormier et al., 1984; Detrick & Purdy, 1980; Minshull et al., 1991; Mutter et al., 1984). In the latter case, ~140 Ma crust is sampled, which may not be representative and comparable to the crustal characteristics across FZs at younger crustal ages. In addition, this FZ has been explored using MCS and ESP seismic data, whereas the other FZs were examined using wide-angle OBS data. In the literature, there are examples of the apparent discrepancy in estimating absolute crustal thickness using reflection versus seismic refraction techniques (e.g., at the East Pacific Rise 9°N: Aghaei et al., 2014; Barth & Mutter, 1996; Canales et al., 2003). Finally, the Blake Spur FZ results were obtained at a transform with a relatively small offset (20 km). If we follow the ridge segmentation nomenclature for slow-spreading mid-ocean ridges proposed by Sempéré et al. (1993), we may classify it as an NTO, rather than a TF, which would then fit within the wide range of crustal thickness observations across several NTOs (Figure 11). In contrast, the thin crust observed for the Kane FZ is puzzling. In fact, the results of Detrick and Purdy (1980) were confirmed by Cormier et al. (1984) after a subsequent, independent survey and data analysis carried out over a 0–25 Ma oceanic crust in the same region. Both studies show the presence of a 2 km thick crust across the FZ, for which we do not have an obvious explanation, except being an indication for a rather magmatically starved segment end.

The difference in crustal thickness within the TF domains observed at slow- versus fast-spreading rates, which we also observe in Figure 11, has been a subject of several studies in the past (e.g., Bai & Montési, 2015; Gregg et al., 2007, 2009; Lin et al., 1990). The presence of thicker crust at fast-spreading centers was commonly attributed to the difference in the available amount of melt, the geometry of the melt region, and the efficiency of melt extraction (Gregg et al., 2007, 2009; Maia, 2018). Our analysis shows that there is a similar order of magnitude of difference in crustal thickness beneath TFs and FZs within slow-spreading environments, which requires further explanations.

The first and almost immediate interpretation one could invoke for this difference is the presence of an increased thickness of the extrusive layer resulting from the pooling of lavas in bathymetry lows toward segment ends within the FZs. Although some accumulation of lavas can be expected around segment ends (e.g., Begnaud et al., 1997; Carbotte & Solomon, 2000; Detrick et al., 1995; Hooft et al., 1997; Marjanović et al., 2018), it is not likely that they can explain >1 km of crustal thickening within the FZ domains. Moreover, in our seismic sections within the Chain FZ, we do not observe the presence of Layer 2A, predominantly built of basalts (Figure 3c). Thus, we consider this explanation unlikely, or at least not as a dominant contributor to the observed differences.

The presence of intense shearing and fracturing along the TFs could be another geological explanation for thinner crust within the TF domains. It is reasonable to expect that at first-order tectonic discontinuities crust thins owing to a combination of factors: shearing, fracturing, and alteration due to hydrothermal

circulation. Once we pass the RTI and transit from transform to FZ domains, these dominant tectonic deformation processes are expected to diminish or completely disappear (Karson & Dick, 1983). However, along TFs within fast-spreading environments, significant thinning of the crust in the TF domain is not observed (Gregg et al., 2007, 2009), even though the zone is characterized by extensive shearing and fracturing, and associated alteration. Although some components of the difference in tectonic activity between the TF and FZ domains may contribute to the observed differences in crustal thickness, we do not consider them as major contributors.

Modeling results presented by Behn et al. (2007) predict cooler thermal structure beneath FZ domains (and warmer beneath TF domains). Therefore, although less extensive shearing and cracking of the oceanic crust are expected within FZ domains, one could speculate that the thermal regime operating beneath FZs could potentially favor serpentinization at greater depths (temperatures $<500\text{--}550^\circ\text{C}$ that are considered as the upper limit for crystallization of serpentine; e.g., Prigent et al., 2020) and result in an apparently thicker crust. As the velocities of gabbros and serpentinized peridotite are similar (e.g., Christensen, 1966, 1972) based on *P*-wave velocity models alone, it would be difficult to distinguish between a scenario in which there would be the presence of serpentinized upper mantle peridotite (with thinner gabbroic crust) and another scenario in which there would be a real excess of gabbroic crust. However, it is well known that the density of these two rock types is different. For instance, peridotite with 25–30% of serpentine would exhibit up to 150 kg/m^3 higher density than gabbro (about the same density difference is valid for serpentinized and unaltered peridotite; e.g., McClymont & Clowes, 2005). A number of earlier studies using 3-D gravity data modeling showed that the TF domains in slow-spreading environments are characterized by positive residual MBA (RMBA) signal (e.g., Blackman & Forsyth, 1991; Detrick et al., 1995; Gregg et al., 2007; Lin et al., 1990). By examining the results from these studies, we notice that most FZ domains are, in contrast, represented by consistently lower RMBAs (e.g., Atlantis transform discontinuity in Gregg et al., 2007). One possible explanation for this observed RMBA pattern could be an excess of gabbroic crust in the FZ domain, which agrees with the results obtained from *P*-wave velocity models. Alternatively, the presence of lower density anomaly beneath FZ domains and higher density anomaly beneath TF domains would be required to explain the same RMBA pattern. The presence of lower density anomaly beneath the FZ domains can be envisaged by replacing peridotite in the upper mantle (density $\sim 3,300\text{ kg/m}^3$) by serpentinized peridotite ($\sim 3,150\text{ kg/m}^3$). On the other hand, to obtain higher RMBA anomaly beneath the TF domains, one would need to replace a portion of the lower gabbroic crust (density $\sim 2,900\text{--}3,000\text{ kg/m}^3$) by serpentinized mantle material. Thus, even by assuming more extensive serpentinization on the FZ side of the RTI, to account for the reported gravity anomalies, we would still need a substantial amount of crustal thickening beneath FZ domains.

To explain the presence of thicker crust within FZs an additional amount of melt would be required. The seafloor fabric, gravity, velocity structure, and presence of extrusives along our profile, together with the ridge axis characteristics reported by Harmon et al. (2018), strongly suggest that the segment north of the Chain transform is magmatically robust (we address this more in detail in section 5.2). One way to extract melt below this ridge segment and to channel it southward to the FZ domain would be through the mechanism of lateral dike propagation: horizontal migration of magma along laterally propagating fractures in the direction parallel to the ridge axis. This mechanism was invoked to explain the observed rapidly migrating earthquake swarms witnessed within different environments associated with volcanism (e.g., Krafla [Iceland]: Brandsdóttir & Einarsson, 1979; Einarsson & Brandsdóttir, 1980; Juan de Fuca Ridge: Bohnenstiehl et al., 2004; Dziak et al., 1995; Fox et al., 1995; offshore Greenland: Callot & Geoffroy, 2004; Afar: Grandin et al., 2012; Keir et al., 2009; Mid-Atlantic Ridge: Giusti et al., 2018). Furthermore, this mechanism was examined by numerical algorithms considering thermal and fluid-mechanical aspects of simulating the flow of magma in an infinite channel and was suggested as a plausible explanation for the crustal thickness variation along slow-spreading ridge segments (Fialko & Rubin, 1998). Finally, there is evidence of lateral dike intrusion at the RTI of a transform system identified in the Cyprus Ophiolite complex (Murton & Gass, 1986). In bathymetry, lateral dike propagation into the older and colder lithosphere across an FZ is observed in the form of so-called overshooting ridge tips forming J-shaped structures, bending toward the transform valley.

J-shaped structures are commonly reported for fast- to intermediate-spreading segments on the FZ side (e.g., Fornari et al., 1989; Gallo et al., 1986; Gregg et al., 2007; Karson et al., 2002; Lonsdale, 1989) and are associated with increased magmatism (Lonsdale, 1994) and crustal thickening (Barth et al., 1994). They have

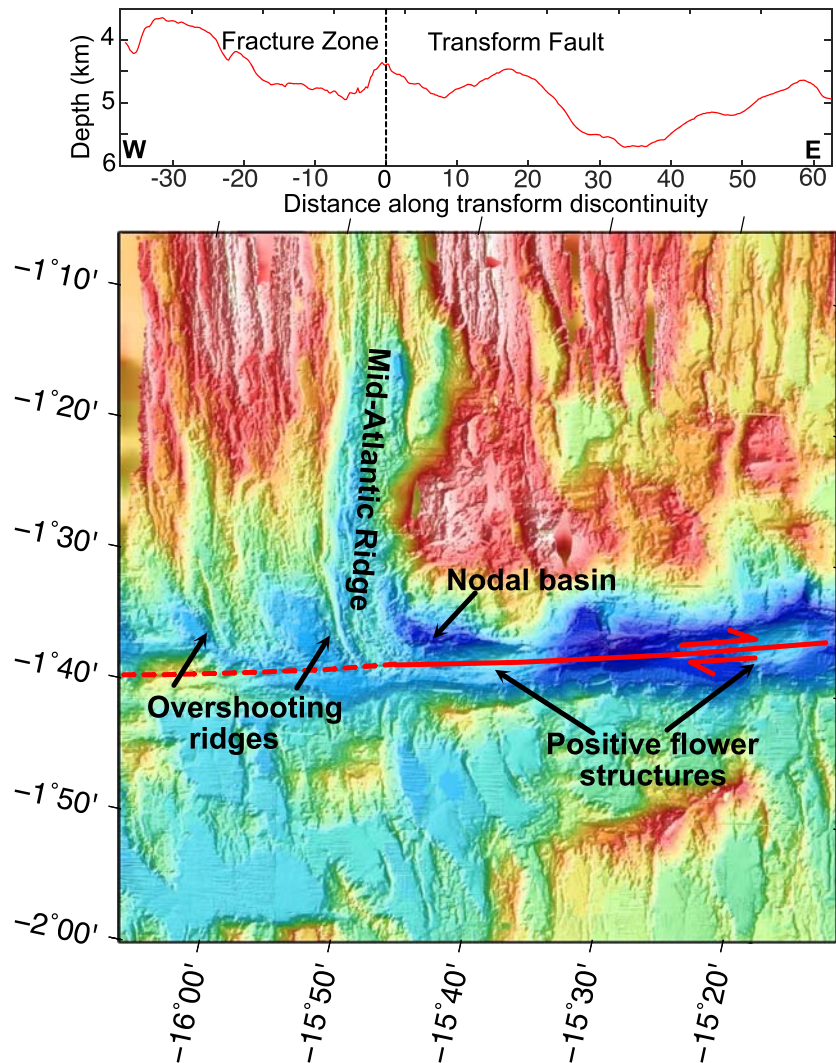


Figure 12. High-resolution bathymetry map (Harmon et al., 2018) focused on the morphotectonic features in the vicinity of the intersection between the Mid-Atlantic Ridge and Chain transform discontinuity. The red line follows the trend of the transform discontinuity: Solid part of the line indicates the transform fault domain, whereas the dashed part of the line indicates the fracture zone domain. Along the same line we extract a bathymetry profile shown in the top. Note the presence of J-shaped structures (labeled “overshooting ridges”) on the fracture zone side of the discontinuity.

also been observed at the equatorial Mid-Atlantic Ridge (Lagabrielle et al., 1992; Ligi et al., 2002; Skolotnev et al., 2020). In the vicinity of the western RTI of the Chain TF in the high-resolution bathymetry data (Harmon et al., 2018), we can identify at least four generations of the J-shaped features (Figure 12), similar to the ones present around the RTIs of some of the fast-spreading transform discontinuities. However, unlike for the J-shape structures within fast-spreading environments where the spacing between two adjacent structures is <5 km, at the Chain RTI, the spacing is almost double. We explain this by the smaller amount of magma available at the slow-spreading MAR segment and longer episodes of tectonic versus magmatically dominated spreading at slow-spreading centers. In global bathymetry data, an arc-like feature comparable to J-shaped structure can be observed on the FZ side of the eastern Chain RTI (Figure 6).

It is interesting to note that dike propagation seems to occur exclusively on the outer corner side of an RTI. Fornari et al. (1989) explained this global observation by the presence of stronger, less fractured lithosphere underlying the outside corner of the RTI. Across the RTI, we do observe that the seafloor within the FZ is

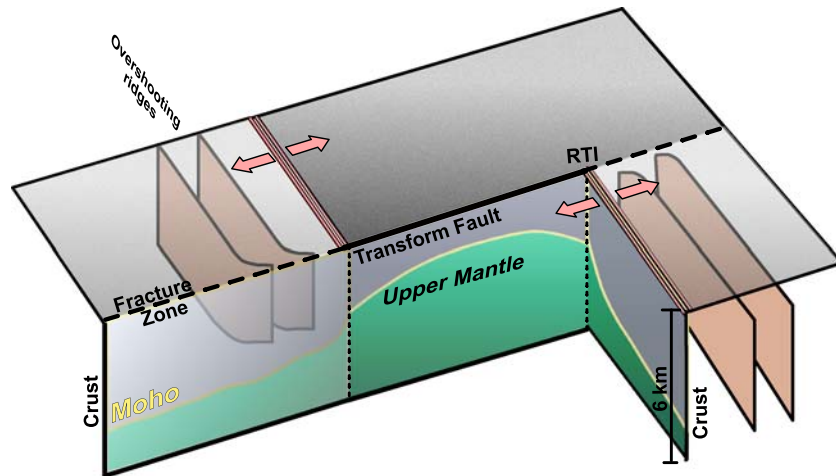


Figure 13. Schematic diagram that depicts lateral dike propagation as our preferred mechanism behind the presence of thicker crust within the fracture zone domain when compared with the transform fault domain.

shallower by >1 km than in the TF domain (Figure 12), potentially providing support for the presence of the weaker crust within the inside corner side. In Figure 13, we provide a schematic view of our preferred model.

In contrast to clear crustal thickness differences between TF and FZ domains, crustal thickness variability associated with the NTOs presented in our compilation (Figure 11) does not show any clear pattern. Mapped crustal thicknesses vary from 2 to 7.2 km (Canales et al., 2000; Dannowski et al., 2018; Davy et al., 2020; Detrick et al., 1993; Dunn et al., 2017; Kahle et al., 2016), including the results from this study. Although the pseudofault crossed by our profile could be considered related to an NTO, we need to emphasize that the crustal thickness variations that are observed across the pseudofaults may not be directly comparable to the global signature of the off-axis trace of an NTO. Pseudofaults may exhibit complexities in crustal thickness as they encompass the zone of transferred, highly deformed older side of the lithospheric block (e.g., Kleinrock & Hey, 1989). A study examining several generations of pseudofaults at the intermediate-spreading Juan de Fuca Ridge (Marjanović et al., 2011) indicated that the crustal structure within the pseudofaults could display reduced crustal thickness due to reduced melt supply at the tip of the propagating segment (Hey et al., 1992; Kruse et al., 2000) and increased shearing and fracturing of the consumed older crust by advancing the propagator's tip (Hooft et al., 1995; Kleinrock & Hey, 1989). The same observation was reported for different spreading rates (Kruse et al., 2000; West et al., 1999). In contrast, it was argued that the younger crust side of the propagator shows an increase in crustal thickness on the scale of several hundred meters to over a kilometer (e.g., Canales et al., 2003; Marjanović et al., 2011), which is interpreted to be due to the higher melt concentration at the base of the crust as a direct consequence of the ridge propagation mechanism (Calvert et al., 1990; Hasselgren et al., 1992; Nedimović et al., 2005). A similar order of thickening is observed for the pseudofault region crossed by our profile, where the crust is ~ 1.2 km thicker within the 20 km wide region of the younger crust side when compared to the zone delimited by the pseudofault. Given that the region is shaped by interleaved processes of ridge propagation, transform faulting, and building up of the transverse ridge (Figure 8) it is not possible to provide further inferences about the presence of thermal/melt anomalies within the upper mantle. In addition, we need to acknowledge that in our model, the crustal thickness/velocity trade-off may be present in our model and that to some extent it may affect our observations.

5.2. Magmatic Versus Tectonic Accretion and Second-Order Segmentation

Bathymetry observations and analyses of the active and passive seismic data indicate that at least five (possibly more) well-defined lower-order segments (delimited either by one first-, and second-order discontinuity or two second-order discontinuities) are present between the Romanche TF and Charcot TF (Figures 1b, 6, and 12). Morphology of these segments suggests that they are in different phases of a volcanotectonic cycle of the seafloor accretion (e.g., Crane & Ballard, 1981; Ito & Behn, 2008; Karson et al., 1987; Stakes et al., 1984; Thibaud et al., 1998). For the two ridge segments offset by the Chain TF (extending directly north and south

of the transform), we suggest that the crust has been forming predominantly by magmatic extension. In contrast, for the segment south of the Romanche TF, a complex tectonic extension phase is dominating the crustal accretion. Finally, the ridge segment south of the 02°10'S NTO Zone seems to represent a transition from predominantly magmatic to tectonic accretion of the crust (going from south to north) with an abrupt change in accretion style at 02°40'45"S. However, for this segment, only a narrow swath of high-resolution bathymetry data is available, and we will not investigate this zone any further.

The second-order segment extending between the Chain TF and ~00°43.5'S (Figures 1b and 12) displays all the characteristics of a magmatically more robust portion of the MAR (Harmon et al., 2018). For most of this segment, bathymetry data show linear volcanic constructions extending almost along the entire length of the segment that, on the western flank (i.e., FZ domain), can be followed southward up to and even over the Chain FZ in the form of overshooting ridges (see section 5.1); it is only within a narrow region extending ~30 km right north of the Chain TF domain that bathymetry suggests a magma-starved zone (Harmon et al., 2018). Based on abyssal hills and imaging of the Layer 2A boundary along our profile, we suggest that the magmatic phase of crustal accretion style has been predominant along this segment for at least the last ~10 Myr. The absence of significant variation in lower crustal velocity (~6.5 km/s; Figure 10) and the absence of variation in crustal thickness may suggest that magma was supplied uniformly from a single upper mantle reservoir along the whole length of this segment. However, it is interesting to note that the observed crustal thickness, 5–6 km, is much thinner when compared to other magmatically robust ridges segments along the MAR, often producing 7–9 km thick crust (e.g., Canales et al., 2000; Dannowski et al., 2011; Hooff et al., 2000).

The ridge segment south of the Chain TF, extending up to the 02°10'N NTO Zone, also shows the presence of well-developed, linear volcanic constructions in the along-axis high-resolution bathymetry data (Figure 6). Along our profile, which runs over ~24 Ma oceanic crust, the segment is shorter due to the ridge propagation that was active at that time (section 4.1; Figure 8). In bathymetry data, remnants of abyssal hills can be partially observed on the younger crust side of the pseudofault (Figure 1c). Within the same region, the base of the Layer 2A/2B boundary can also be identified intermittently (Figure 3f). Although spatially limited, these observations suggest that this segment most probably has been magmatically more robust at least for the past 24 Myr and possibly from the very onset of the propagation.

When we compare these two magmatically more robust segments along our profile, we see differences in the FAA signal and in the seafloor depth (Figure 2). The younger lithospheric block (north of the Chain FZ) is characterized by a ~40 mGal higher gravity signal and ~700 m shallower seafloor ($3,710 \pm 100$ and $4,380 \pm 190$ m, north and south of the Chain FZ, respectively; Figure 2). To assess whether this difference in the seafloor depth/gravity could be explained by the age-dependent subsidence rate of the juxtaposed lithospheric blocks of different ages, 10 Ma in the north versus 24 Ma in the south (Müller et al., 2008), we use one of the linear relationships between the depth to the seafloor and age, available in the literature (e.g., DeLong et al., 1977):

$$D = 0.336\sqrt{t} + C,$$

where D is the depth to the seafloor, t is the age of the examined lithosphere, and C is a constant that represents the depth of the ridge axis, normally the shallowest point of the ridge axis (DeLong et al., 1977). For the region north of the Chain FZ, where we assume the presence of 10 Ma old lithosphere (Müller et al., 2008) and $2,650 \pm 50$ m as an average minimum depth of the ridge axis, the predicted range of seafloor depth is 3,660–3,760 m. Similarly, for the region south of the Chain FZ, assuming the same average depth of the ridge axis and 24 Ma old lithosphere (Müller et al., 2008), we obtain the predicted depth range to be 4,250–4,350 m. The results of this simplified age-seafloor depth relationship indicate that, within the accuracy of the assumed variables and standard deviation of seafloor depth, we can explain the observed difference in seafloor depth. This further suggests that these two segments may be underlain by a relatively similar thermal/magmatic regime in the lithosphere. However, the standard deviation of seafloor depth south of the Chain FZ is relatively high, and this may reflect the presence of some small-scale heterogeneities in mantle composition.

An earlier geochemical study conducted on basaltic glasses from the axial region, including analyses of major elements, REE and isotopes, evidenced a continuous and gradual geochemical enrichment from the

Charcot to Romanche TFs (Schilling et al., 1994, 1995). The presence of this gradual trend was interpreted as a mixing zone, that is, transition-type mid-ocean ridge basalts (T-type MORB) between the region of normal-type (N-type) MORB south of the Charcot TF and enriched-type (E-type) MORB north of the St. Paul TF. Within these three, large-scale chemically distinct zones, local heterogeneities are nested. Along the transition zone, which matches the extent of the zone we examine in this study, clustering in geochemical signatures that corresponds to the extent of the second-order tectonic discontinuities seems to be evident. For instance, the magmatically robust segment extending directly north of the Chain TF, as well as the ridge segments extending between the Chain TF and the 02°10'S NTO, shows a large variability in major elements, Na₂O and K₂O, in La/Sm and Nd-Pb-Sr isotope ratios (Schilling et al., 1994). The same hold true for the segments extending between the Chain TF and 02°10'S NTO Zone. This spatial correlation leads us to propose that the presence of the enriched relatively small bodies within depleted asthenosphere responsible for the observed geochemical pattern (Schilling et al., 1994) may govern the second-order tectonic segmentation within the equatorial Atlantic region, which agrees with the view proposed by Macdonald et al. (1988).

It is important to mention that by carefully reexamining the available geochemical profiles (Le Voyer et al., 2015; Schilling et al., 1994, 1995), we find that the abrupt change between the N- and T-type MORBs seems to be collocated with the 02°10'S NTO Zone, not the Charcot TF. In fact, more abrupt changes in isotopes, REE, and most of volatile contents (except S and CO₂) are observed at the 02°10'S NTO Zone, rather than at the Chain or Charcot TFs. Although this observation does not change the global view on the geochemical complexity of the equatorial Atlantic mantle, it may have an important implication on our understanding of the role of NTOs in the lithosphere/asthenosphere magma mixing and thermal properties. Even though the NTOs represent second-order ridge discontinuities they may be deeply rooted, and their effect should not be neglected in numerical models.

In contrast to these two magmatically more robust segments, the segment extending between the Romanche TF and 00°43.5'S seems to be magmatically starved. Seafloor bathymetry displays an obliquely trending (Figure 1b), en échelon segmented ridge axis without a well-developed axial valley (Bonatti et al., 2001). Along our profile that samples an approximately 7 Ma lithosphere (Müller et al., 2008), this segment is characterized by a deeper seafloor when compared to the segment just to the south (Figure 2), indicating the presence of a colder lithospheric regime (Bonatti et al., 1994; Dalton et al., 2014). Moreover, in the seismic reflection data, we do not observe the presence of the Layer 2A/2B event (Figure 3c), suggesting a tectonically dominated spreading. Along the 2-D velocity profile, the lower crustal velocities north of 00°43.5'S are significantly higher than that for the southern magmatically more robust segment (Figure 9c). In fact, the lower crustal velocities we observe for the northern segment are comparable to upper mantle velocities, that is, exhumed peridotite velocities (>7.5 km/s). The predominant presence of exposed peridotites and gabbros is revealed in the samples dredged from the seafloor for about the same stretch of the segment, ~50 km south of the Romanche TF (Bonatti et al. 2001; Bonatti, Ligi, Carrara, et al., 1996). In addition, the examined peridotite samples are represented by an atypically low degree of melting, which was interpreted as the evidence for the existence of the cold spot in the equatorial Atlantic region (Bonatti et al., 1994, 2001; Dalton et al., 2014). We need to mention that for this region we observe relatively higher average crustal thickness (>6 km), when compared to the magmatically robust southern segment (5.1 km; Figures 9 and 10). This is in contrast to the common notion of a thicker crust along magmatically robust portion of a ridge axis. Besides complex tectonic processes, and extensive serpentization (Bonatti et al., 2001) that may be present and result in apparent crustal thickening, we need to acknowledge the fact that the crustal thickness/velocity trade-off may be partially responsible for these observations. A separate study focused on the Romanche TF is being conducted (Gregory et al., 2020), and the results will be presented elsewhere.

5.3. The Origin of the Transverse Ridge

Transverse ridges associated with transform discontinuities are commonly observed features across spreading rates, running parallel to TFs and/or along the older lithospheric block of an FZ domain (Abrams et al., 1988; Bonatti, 1978; Bonatti & Honnorez, 1976; Bonatti et al., 2005; Cannat et al., 1991; Detrick & Purdy, 1980; Dick et al., 1991; Kastens et al., 1998; Maia, 2018; Potts, Calvert, et al., 1986; Tucholke & Schouten, 1988; Whitmarsh & Calvert, 1986). The most prominent transverse ridges are associated with slow slip environments along the MAR, such as the one we observe on the older crust side of the Chain FZ. Although they represent major bathymetric features, the mechanism behind their formation is not clear.

A number of hypotheses have been proposed to explain their nature (e.g., Abrams et al., 1988; Kastens et al., 1998). Even in the early stages of geophysical and petrological exploration of conservative plate boundaries, it was clear that transverse ridges are not the result of constructive volcanism (e.g., Abrams et al., 1988; Bonatti, 1978), as an asymmetry in shape and highly tectonized crust were reported for the majority of examined cases. Instead, the existence of vertical movement of lithospheric fragments was proposed as the most plausible mechanism. However, the governing processes that lead to this vertical uplift are still debated (e.g., Bonatti et al., 2005; Pockalny et al., 1997; Tucholke & Schouten, 1988).

Differential subsidence (Parmentier & Haxby, 1986; Sandwell, 1984; Sandwell & Schubert, 1982) has been invoked to explain the origin of the uplifted features along transform discontinuities. One group of thermo-mechanical models (Sandwell, 1984; Sandwell & Schubert, 1982) suggested that differential subsidence results in stresses that are expressed in flexing of the lithosphere and development of uplift on the younger side of the transform. However, our observations at the Chain FZ (Figure 1b) and the observations coming from other transform discontinuities along the MAR show that the transverse ridges are not observed on the younger lithospheric block side (e.g., Abrams et al., 1988; Bonatti, 1978; Gasperini et al., 2017; Tucholke & Schouten, 1988). In contrast, Parmentier and Haxby (1986) presented theoretical models that involve thermal bending moments governed by the lithosphere thickness and age, which cause the older side to flex and create a topographic high. If this mechanism was predominant, we would expect similar uplift to occur on both flanks. However, in most cases, we see uplift only on one of the flanks.

Horizontal thermal conduction from the younger to the older lithospheric block across transform/FZ domains (Forsyth & Wilson, 1984; Langseth & Hobart, 1976; Louden & Forsyth, 1976) is another mechanism that has been used to explain systematic changes in thermotectonic structure, as well as variations in depth of the seafloor in the vicinity of FZs (Morgan & Forsyth, 1988). Chen (1988) evaluated the extent of the uplift assuming two thermal contributions: lateral heat conduction across the transform and anomaly due to shear heating. According to this model, assuming 15–20 Ma age difference (comparable to what we observe for the Chain FZ), the expected uplift along the older lithospheric block would be ~600 m. This prediction is in contrast with the seafloor observations, which show that transverse ridges raise to a couple of thousands of meters above the surrounding seafloor, as for the transverse ridge we observe along the Chain FZ (Figures 1b and 2). In addition, the question of why the transverse ridges are often observed only on one of the flanks, here on the southern flank, cannot be addressed by this hypothesis either.

As transform discontinuities represent regions of intense fracturing, it is reasonable to envisage the presence of serpentinization resulting from the alteration of upper mantle peridotite in contact with seawater. The serpentinite would form diapirs due to its lower density and would rise upwards intruding the overlying crust, that is, serpentine diapirism (e.g., Bonatti & Honnorez, 1976; Bonatti, 1978; Francis, 1981), causing the uplift. Although samples of a serpentinized mantle have been dredged along different transform domains (e.g., Bonatti, 1978; Bonatti et al., 2001; Cannat et al., 1991) we do not observe any indication for intense serpentinization across the transverse ridge in our velocity profile (Figure 9b). In fact, beneath the transverse ridge, the crustal thickness, as well as the lower crustal velocity, is comparable to the values reported for a typical oceanic crust formed within the slow-spreading environment (e.g., Grevemeyer et al., 2018). The velocity contours suggest that the northern wall could be represented predominantly by exposed dikes and/or gabbros. Similar observations in seismic velocities were reported by earlier seismic refraction studies (e.g., Potts, White, et al., 1986; Whitmarsh & Calvert, 1986). To explain the lack of a serpentinization signal in velocity models, the argument that serpentinite might show compressional velocity and density similar to fractured metagabbros that constitute lower oceanic crust has been used (Cannat et al., 1991; Carlson & Miller, 1997). However, in the presence of significant serpentinization, upper mantle velocities should be at least ~200 m/s lower than typical values (e.g., McClymont & Clowes, 2005), which is the opposite of what we observe here. The region beneath the transverse ridge displays rather high velocities in the upper crust, ~5.8 km/s (Figure 10), and has been densely sampled by Pg arrivals (Figure S6). Moreover, Minshull et al. (1991) determined that even if we assume isostatically compensated crust with 3 km thick serpentinized peridotite, the resulting uplift would be only on the order of 200–300 m. Even though some amount of serpentinization may exist in the form of thin veins that fill in cracks and fissures, which we cannot image in our tomography model, it does not seem to represent an important factor in the formation of the transverse ridge.

In addition to the thermomechanical hypotheses to explain the formation of transverse ridges, a number of mechanisms involving viscodynamic forces as a major factor have also been proposed. For instance, the mechanism suggested by Collette (1986) argues that transverse ridges result from asthenosphere upwelling beneath the transform valley, causing bending of the transform walls. Another hypothesis proposed that asthenosphere upwelling beneath the ridge axis induces drag forces and bending of the old lithosphere in the vicinity of the transform (Sleep & Biehler, 1970). The former hypothesis poses the same problems as the thermomechanical models we discussed earlier (e.g., why would a transverse ridge develop on only one side of the transform valley and at some distance from the RTI?). However, the latter hypothesis could be viable in the case of transform boundaries that offset segments with different magmatic budgets (e.g., more magmatically robust in the north and more magmatically starved in the south and vice versa). In the case of the Chain TF, both the north and ridge segments, offset by the Chain TF, seem to display all the characteristics of more magmatically robust segments (section 5.2), and therefore, it is hard to envisage the scenario in which the development of the transverse ridge would be possible only on the western flank. However, to completely rule out this possibility, additional studies regarding asthenospheric flow beneath FZ domains need to be conducted.

We finally consider a combination of compressional and extensional forces due to changes in relative plate motion that has been proposed as the dominant mechanism to explain the formation of the observed transverse ridges (Bonatti, 1978; Bonatti et al., 1994; Mauduit & Dauteuil, 1996; Menard & Atwater, 1969; Pockalny, 1997). Following the FZ geometry and location of the transverse ridge, this mechanism provides the most plausible explanation for the formation of the transverse ridge along the Chain FZ (Figure 8). At ~46–38 Ma, a significant reorganization of plates took place and resulted in a change of the FZ orientation of ~8°. Following Bonatti (1978), we suggest that this change in plate orientation introduced significant compressional forces on the FZ domain west of the Chain TF's western RTI and extensional forces on the northern wall of the Chain transform domain (Figure 8). Moreover, it was probably this prominent change in plate orientation that ceased the lengthening of the ridge segment north of the Chain TF (from 130 km at 70 Ma to 200 km at ~46 Ma) and triggered the southward propagation of the ridge segment south of the Chain TF. This propagation could have also influenced local field stresses and contributed to a more prominent uplift of the transverse ridge in its westernmost portion (Figure 8). It is also interesting to note that the spreading rate between 30 and 20 Ma increased to ~26 mm/yr, which roughly coincides with the activity of the propagator.

Bonatti et al. (2005) performed numerical modeling to show that the transverse ridge formed along the Vema transform discontinuity is a result of lithospheric flexure due to extension within the transform coinciding with the shift in the orientation of the MAR by 5–10° ~11–12 Ma. A similar scenario was proposed for the Clipperton TF (Pockalny et al., 1997). However, for the transverse ridge along the Kane FZ, while thermal heating of the lithosphere is proposed to govern the uplift, the primary trigger mechanism was the episodes of large plate kinematic changes, notably between 92 and 59 Ma (Tucholke & Schouten, 1988). At the Chain FZ, from the coincident formation of the transverse ridge and initiation of ridge propagation (Figure 8), we suggest that the change in plate motion was the governing process. A combination of other processes, including the ones we have discussed such as the lithospheric flexure, and/or thermal heating, could have acted simultaneously and contributed to the uplift. However, which of these additional processes and to what extent they have participated in shaping the transverse ridge are not possible to define with the given data sets.

6. Conclusions

Our data analyses focused on the Chain transform system, together with a handful of data available in the literature sampling this zone (Harmon et al., 2018; Le Voyer et al., 2015; Schilling et al., 1994, 1995), provide us with insights on the morphotectonic characteristics of the area. Based on the bathymetry and seismic reflection data, we corroborate the presence of a long-lived (at least for the past 10 Ma) magmatically more robust ridge segment extending north of the Chain TF to ~00°43.5'S. Also, we suggest that an equally magmatically robust ridge segment is extending south of the Chain TF to the NTO 02°10'S. We identify and describe crustal properties and seafloor expressions of the morphotectonic features: the Chain FZ, transverse ridge, and pseudofault formed by southward propagation of the segment south of the Chain TF. In addition

to reporting on the local geological setting, our newly acquired information, in combination with the existing studies, helps us to better understand FZs globally.

1. The compilation of the crustal thicknesses across slow-slipping transform discontinuity systems show that the crust within FZ domains in a slow-spreading ridge environment on a global level, including the Chain FZ, does not show evidence for significant crustal thinning, which characterizes most of the TFs. To explain the presence of “close to normal” thickness of oceanic crustal thickness (~5 km on average) within FZs, we propose lateral dike propagation as the dominant mechanism. This interpretation is supported by the observations of well-developed J-shaped structures in the bathymetry data, indicating that the crustal accretion process at RTIs may not be spreading rate dependent as suggested by Gregg et al. (2007).
2. The off-axis wakes formed behind the NTOs (second-order tectonic discontinuities) do not show any consistent pattern in terms of their crustal thicknesses. A wide range of the observed thicknesses suggests that other processes may have an important impact on shaping the crust formed at the NTOs, such as ridge propagation.
3. Based on our results, together with the compilation of geochemical studies (Le Voyer et al., 2015; Schilling et al., 1994, 1995), we suggest that NTOs as second-order discontinuities may have an important role in the tectonomagmatic segmentation of the lithosphere. They can be considered as vertical lithospheric barriers that are rooted deeper, potentially at the base of the lithosphere and possibly controlled by deep-seated asthenospheric magma anomalies. Our findings suggest that the effect of the NTOs should not be neglected in numerical modeling.
4. Based on the location and the onset of the transverse ridge observed on the older lithospheric block of the Chain FZ, and in combination with the findings from earlier studies, we suggest that a major reorganization in plate motion represents the primary triggering mechanism for building up transverse ridges. Besides the dominant factor of plate reorientation, other additional factors may contribute to the uplift, such as lithospheric flexure and thermal heating.

Data Availability Statement

The MCS data sets are processed using Paradigm software package. The data presented in the paper are archived at Pangea (<https://doi.pangaea.de/10.1594/PANGAEA.922331>).

Acknowledgments

We would like to acknowledge the crews during TransAtlantic ILAB, LITHOS, and ILAB-SPARC survey, for their work that led to successful data collection. We are grateful to WesternGeco Processing Team. We would also like to thank Christine Deplus for the help with the processing of the raw gravity data. We wish to thank Juan Pablo Canales, Marco Ligi, and the associate editor for their constructive comments and suggestions that improved the manuscript. This project is funded by the European Research Council Advanced Grant Agreement 339442 TransAtlantic ILAB.

References

- Abrams, L. J., Detrick, R. S., & Fox, P. J. (1988). Morphology and crustal structure of the Kane fracture zone transverse ridge. *Journal of Geophysical Research*, 93(B4), 3195–3210. <https://doi.org/10.1029/JB093iB04p03195>
- Aghaei, O., Nedimović, M. R., Carton, H., Carbotte, S. M., Canales, J. P., & Mutter, J. C. (2014). Crustal thickness and Moho character of the fast-spreading East Pacific Rise from 9°42'N to 9°57'N from post-stack migrated 3-D MCS data. *Geochemistry, Geophysics, Geosystems*, 15, 634–657. <https://doi.org/10.1002/2013GC005069>
- Ambos, E. L., & Hussong, D. M. (1986). Oceanographer transform fault structure compared to that of surrounding oceanic crust: Results from seismic refraction data analysis. *Journal of Geodynamics*, 5, 79–102. [https://doi.org/10.1016/0264-3707\(86\)90024-4](https://doi.org/10.1016/0264-3707(86)90024-4)
- Antolik, M., Abercrombie, R. E., Pan, J., & Ekström, G. (2006). Rupture characteristics of the 2003 M_w 7.6 mid-Indian Ocean earthquake. *Journal of Geophysical Research*, 111, B04302. <https://doi.org/10.1029/2005JB003785>
- Audhkhasi, P., & Singh, S. C. (2019). Seismic structure of the upper crust from 0–75 Ma in the equatorial Atlantic Ocean on the African Plate using ultra-long offset seismic data. *Geochemistry, Geophysics, Geosystems*, 20, 6140–6162. <https://doi.org/10.1029/2019GC008577>
- Auffret, Y., Pelleau, P., Klingelhoefer, F., Géli, L., Crozon, J., Lin, J., & Sibuet, J. C. (2004). MicroOBS: A new generation of ocean bottom seismometer. *First Break*, 22(7). <https://doi.org/10.3997/1365-2397.2004012>
- Bai, H., & Montési, L. G. (2015). Slip-rate-dependent melt extraction at oceanic transform faults. *Geochemistry, Geophysics, Geosystems*, 16, 401–419. <https://doi.org/10.1002/2014GC005579>
- Barth, G. A., Kastens, K. A., & Klein, E. M. (1994). The origin of bathymetric highs at ridge-transform intersections: A multi-disciplinary case study at the Clipperton Fracture Zone. *Marine Geophysical Researches*, 16(1), 1–50. <https://doi.org/10.1007/BF01812444>
- Barth, G. A., & Mutter, J. C. (1996). Variability in oceanic crustal thickness and structure: Multichannel seismic reflection results from the northern East Pacific Rise. *Journal of Geophysical Research*, 101, 17,951–17,975. <https://doi.org/10.1029/96JB00814>
- Batiza, R. (1981). Lithospheric age dependence of off-ridge volcano production in the North Pacific. *Geophysical Research Letters*, 8(8), 853–856. <https://doi.org/10.1029/GL008i008p00853>
- Batiza, R. (1982). Abundances, distribution and sizes of volcanoes in the Pacific Ocean and implications for the origin of non-hotspot volcanoes. *Earth and Planetary Science Letters*, 60, 195–206. [https://doi.org/10.1016/0012-821X\(82\)90003-6](https://doi.org/10.1016/0012-821X(82)90003-6)
- Begnaud, M. L., McClain, J. S., Barth, G. A., Orcutt, J. A., & Harding, A. J. (1997). Velocity structure from forward modeling of the eastern ridge-transform intersection area of the Clipperton Fracture Zone, East Pacific Rise. *Journal of Geophysical Research*, 102, 7803–7820. <https://doi.org/10.1029/96JB03393>

- Behn, M. D., Boettcher, M. S., & Hirth, G. (2007). Thermal structure of oceanic transform faults. *Geology*, *35*(4), 307–310. <https://doi.org/10.1130/G23112A.1>
- Bell, R. E., & Buck, W. R. (1992). Crustal control of ridge segmentation inferred from observations of the Reykjanes Ridge. *Nature*, *357*, 583–586. <https://doi.org/10.1038/357583a0>
- Bird, P. (2003). An updated digital model of plate boundaries. *Geochemistry, Geophysics, Geosystems*, *4*(3), 1027. <https://doi.org/10.1029/2001GC000252>
- Blackman, D. K., & Forsyth, D. W. (1991). Isostatic compensation of tectonic features of the Mid-Atlantic Ridge: 25°–27°30'S. *Journal of Geophysical Research*, *96*, 11,741–11,758. <https://doi.org/10.1029/91JB00602>
- Bohnenstiehl, D. R., Dziak, R. P., Tolstoy, M., Fox, C. G., & Fowler, M. (2004). Temporal and spatial history of the 1999–2000 Endeavour Segment seismic series, Juan de Fuca Ridge. *Geochemistry, Geophysics, Geosystems*, *5*, Q09003. <https://doi.org/10.1029/2004GC000735>
- Bonatti, E. (1978). Vertical tectonism in oceanic fracture zones. *Earth and Planetary Science Letters*, *37*, 369–379. [https://doi.org/10.1016/0012-821X\(78\)90052-3](https://doi.org/10.1016/0012-821X(78)90052-3)
- Bonatti, E., Brunelli, D., Buck, W. R., Cipriani, A., Fabretti, P., Ferrante, V., et al. (2005). Flexural uplift of a lithospheric slab near the Vema transform (Central Atlantic): Timing and mechanisms. *Earth and Planetary Science Letters*, *240*, 642–655. <https://doi.org/10.1016/j.epsl.2005.10.010>
- Bonatti, E., Brunelli, D., Fabretti, P., Ligi, M., Portaro, R. A., & Seyler, M. (2001). Steady-state creation of crust-free lithosphere at cold spots in mid-ocean ridges. *Geology*, *29*(11), 979–982. [https://doi.org/10.1130/0091-7613\(2001\)029%3C0979:SSCOCF%3E2.0.CO;2](https://doi.org/10.1130/0091-7613(2001)029%3C0979:SSCOCF%3E2.0.CO;2)
- Bonatti, E., & Crane, K. (1982). Oscillatory spreading explanation of anomalously old uplifted crust near oceanic transforms. *Nature*, *300*, 343–345. <https://doi.org/10.1038/300343a0>
- Bonatti, E., & Honnorez, J. (1976). Sections of the following conclusions: Earth's crust in the equatorial Atlantic. *Journal of Geophysical Research*, *81*, 4104–4116. <https://doi.org/10.1029/JB081i023p04104>
- Bonatti, E., Ligi, M., Borsetti, A., Gasperini, L., Negri, A., & Sartori, R. (1996). Lower Cretaceous deposits trapped near the equatorial Mid-Atlantic Ridge. *Nature*, *380*(6574), 518–520. <https://doi.org/10.1038/380518a0>
- Bonatti, E., Ligi, M., Carrara, G., Gasperini, L., Turko, N., Perfiliev, S., et al. (1996). Diffuse impact of the Mid-Atlantic Ridge with the Romanche transform: An ultracold ridge-transform intersection. *Journal of Geophysical Research*, *101*(B4), 8043–8054. <https://doi.org/10.1029/95JB02249>
- Bonatti, E., Ligi, M., Gasperini, L., Peyve, A., Raznitsin, Y., & Chen, Y. J. (1994). Transform migration and vertical tectonics at the Romanche fracture zone, equatorial Atlantic. *Journal of Geophysical Research*, *99*(B11), 21,779–21,802. <https://doi.org/10.1029/94JB01178>
- Bonatti, E., Raznitsin, Y., Bortoluzzi, G., Budillon, F., De Alteriis, G., Gasperini, L., et al. (1991). *Geological studies of the eastern part of the Romanche transform (equatorial Atlantic): A first report*, *Giornale di Geologia*, ser. 3 (Vol. 53/2, pp. 31–48). Bologna.
- Brandsdóttir, B., & Einarsson, P. (1979). Seismic activity associated with the September 1977 deflation of the Krafla Central Volcano in Northeastern Iceland. *Journal of Volcanology and Geothermal Research*, *6*, 197–212. [https://doi.org/10.1016/0377-0273\(79\)90001-5](https://doi.org/10.1016/0377-0273(79)90001-5)
- Callot, J. P., & Geoffroy, L. (2004). Magma flow in the East Greenland dyke swarm inferred from study of anisotropy of magnetic susceptibility: Magmatic growth of volcanic margin. *Geophysical Journal International*, *159*(2), 816–830. <https://doi.org/10.1111/j.1365-246X.2004.02426.x>
- Calvert, A. J., Hasselgren, E. A., & Clowes, R. M. (1990). Oceanic rift propagation—A cause of crustal underplating and seamount volcanism. *Geology*, *18*(9), 886–889. [https://doi.org/10.1130/0091-7613\(1990\)018%3C0886:ORPACO%3E2.3.CO;2](https://doi.org/10.1130/0091-7613(1990)018%3C0886:ORPACO%3E2.3.CO;2)
- Calvert, A. J., & Potts, C. (1985). Seismic evidence for hydrothermally altered mantle beneath old crust in the Tydeman fracture zone. *Earth and Planetary Science Letters*, *75*, 439–449. [https://doi.org/10.1016/0012-821X\(85\)90187-6](https://doi.org/10.1016/0012-821X(85)90187-6)
- Canales, J. P., Detrick, R. S., Lin, J., Collins, J. A., & Toomey, D. R. (2000). Crustal and upper mantle seismic structure beneath the rift mountains and across a non-transform offset at the Mid-Atlantic Ridge (35°N). *Journal of Geophysical Research*, *105*(B2), 2699–2719. <https://doi.org/10.1029/1999JB900379>
- Canales, J. P., Detrick, R. S., Toomey, D. R., & Wilcock, W. S. D. (2003). Segment-scale variations in the crustal structure of 150–300 kyr old fast spreading oceanic crust (East Pacific Rise, 8°15'N–10°5'N) from wide-angle seismic refraction profiles. *Geophysical Journal International*, *152*, 766–794. <https://doi.org/10.1046/j.1365-246X.2003.01885.x>
- Cannat, M., Mamaloukas-Frangoulis, V., Auzende, J. M., Bideau, D., Bonatti, E., Honnorez, J., et al. (1991). A geological cross-section of the Vema fracture zone transverse ridge. *Journal of Geodynamics*, *13*, 97–118. [https://doi.org/10.1016/0264-3707\(91\)90034-C](https://doi.org/10.1016/0264-3707(91)90034-C)
- Carbotte, M., & Solomon, A. (2000). Evaluation of morphological indicators of magma supply and segmentation from a seismic reflection study of the East Pacific Rise 15°30'–17°N. *Journal of Geophysical Research*, *105*(B2), 2737–2759. <https://doi.org/10.1029/1999JB900245>
- Carbotte, S. M., Smith, D. K., Cannat, M., & Klein, E. M. (2015). Tectonic and magmatic segmentation of the Global Ocean Ridge System: A synthesis of observations. In T. J. Wright, A. Ayele, D. J. Ferguson, T. Kidane, C. Vye-Brown (Eds.), *Magmatic rifting and active volcanism, Special Publications* (Vol. 420, pp. 249–295). London: Geological Society. <https://doi.org/10.1144/SP420.5>
- Carlson, R., & Miller, J. (1997). A new assessment of the abundance of serpentinites in the oceanic crust. *Geophysical Research Letters*, *24*, 457–460. <https://doi.org/10.1029/97GL00144>
- Chen, Y. (1988). Thermal model of oceanic transform faults. *Journal of Geophysical Research*, *93*(B8), 8839–8851. <https://doi.org/10.1029/JB093iB08p08839>
- Chen, Y. J. (1992). Oceanic crustal thickness versus spreading rate. *Geophysical Research Letters*, *19*, 753–756. <https://doi.org/10.1029/92GL00161>
- Christensen, N. I. (1966). Elasticity of ultrabasic rocks. *Journal of Geophysical Research*, *71*, 5921–5931. <https://doi.org/10.1029/JZ071i024p05921>
- Christensen, N. I. (1972). The abundance of serpentinites in the oceanic crust. *Journal of Geology*, *80*, 709–719. <https://www.jstor.org/stable/30080142>
- Christeson, G. L., Goff, J. A., & Reece, R. S. (2019). Synthesis of oceanic crustal structure from two-dimensional seismic profiles. *Reviews of Geophysics*, *57*, 504–529. <https://doi.org/10.1029/2019RG000641>
- Collette, B. J. (1986). Fracture zones in the North Atlantic: Morphology and a model. *Journal of the Geological Society*, *143*, 763–774. <https://doi.org/10.1144/gsjgs.143.5.0763>
- Cormier, M. H., Detrick, R. S., & Purdy, G. M. (1984). Anomalously thin crust in oceanic fracture zones: New seismic constraints from the Kane fracture zone. *Journal of Geophysical Research*, *89*, 10,249–10,266. <https://doi.org/10.1029/JB089iB12p10249>
- Crane, K., & Ballard, R. D. (1981). Volcanics and structure of the famous Nargowgate rift: Evidence for cyclic evolution: AMAR 1. *Journal of Geophysical Research*, *86*, 5112–5124. <https://doi.org/10.1029/JB086iB06p05112>

- Creager, K. C., & Dorman, L. M. (1982). Location of instruments on the seafloor by joint adjustment of instrument and ship positions. *Journal of Geophysical Research*, *87*, 8379–8388. <https://doi.org/10.1029/JB087iB10p08379>
- Dalton, C. A., Langmuir, C. H., & Gale, A. (2014). Geophysical and geochemical evidence for deep temperature variations beneath mid-ocean ridges. *Science*, *344*, 80–83. <https://doi.org/10.1126/science.1249466>
- Dannowski, A., Grevemeyer, I., Phipps Morgan, J., Ranero, C. R., Maia, M., & Klein, G. (2011). Crustal structure of the propagating TAMMAR ridge segment on the Mid-Atlantic Ridge, 21.5°N. *Geochemistry, Geophysics, Geosystems*, *12*, Q07012. <https://doi.org/10.1029/2011GC003534>
- Dannowski, A., Morgan, J. P., Grevemeyer, I., & Ranero, C. R. (2018). Enhanced mantle upwelling/melting caused segment propagation, oceanic core complex die off, and the death of a transform fault: The Mid-Atlantic Ridge at 21.5°N. *Journal of Geophysical Research: Solid Earth*, *123*, 941–956. <https://doi.org/10.1002/2017JB014273>
- Davy, R. G., Collier, J. S., & Henstock, T. J. (2020). Wide-angle seismic imaging of two modes of crustal accretion in mature Atlantic Ocean crust. *Journal of Geophysical Research: Solid Earth*, *125*, e2019JB019100. <https://doi.org/10.1029/2019JB019100>
- DeLong, S. E., Dewey, J. F., & Fox, P. J. (1977). Displacement history of oceanic fracture zones. *Geology*, *5*, 199–202. [https://doi.org/10.1130/0091-7613\(1977\)5%3C199:DHOOFZ%3E2.0.CO;2](https://doi.org/10.1130/0091-7613(1977)5%3C199:DHOOFZ%3E2.0.CO;2)
- Detrick, R. S., Cormier, M. H., Prince, R. A., Forsyth, D. W., & Ambos, E. L. (1982). Seismic constraints on the crustal structure of the Vema fracture zone. *Journal of Geophysical Research*, *87*, 599–610. <https://doi.org/10.1029/JB087iB13p10599>
- Detrick, R. S., Needham, H. D., & Renard, V. (1995). Gravity-anomalies and crustal thickness variations along the Mid-Atlantic Ridge between 33°N and 40°N. *Journal of Geophysical Research*, *100*, 3767–3787. <https://doi.org/10.1029/94JB02649>
- Detrick, R. S., & Purdy, G. M. (1980). The crustal structure of the Kane fracture zone from seismic refraction studies. *Journal of Geophysical Research*, *85*, 3759–3778. <https://doi.org/10.1029/JB085iB07p03759>
- Detrick, R. S., White, R. S., & Purdy, G. M. (1993). Crustal structure of North Atlantic Fracture Zones. *Reviews of Geophysics*, *31*(4), 439–458. <https://doi.org/10.1029/93RG01952>
- Dick, H. J. B., Schouten, H., Meyer, P. S., Gallo, D. G., Berg, H., Tyce, R., et al. (1991). Tectonic evolution of the Atlantis II fracture zone. *Proc. Ocean Drilling Program, Scientific Results*, *118*, 359–398.
- Dunn, R. A., Arai, R., Eason, D. E., Canales, J. P., & Sohn, R. A. (2017). Three-dimensional seismic structure of the Mid-Atlantic Ridge: An investigation of tectonic, magmatic, and hydrothermal processes in the rainbow area. *Journal of Geophysical Research: Solid Earth*, *122*, 9580–9602. <https://doi.org/10.1002/2017JB015051>
- Dziak, R. P., Fox, C. G., & Schreiner, A. E. (1995). The June–July 1993 seismo-acoustic event at CoAxial segment, Juan de Fuca Ridge: Evidence for a lateral dike injection. *Geophysical Research Letters*, *22*, 135–138. <https://doi.org/10.1029/94GL01857>
- Einarsson, P., & Brandsdóttir, B. (1980). Seismological evidence for lateral magma intrusion during the July 1978 deflation of the Krafla volcano in NE-Iceland. *Journal of Geophysics*, *47*, 160–165. <https://doi.org/10.2172/890964>
- Fialko, Y. A., & Rubin, A. M. (1998). Thermodynamics of lateral dike propagation: Implications for crustal accretion at slow spreading mid-ocean ridges. *Journal of Geophysical Research*, *103*(B2), 2501–2514. <https://doi.org/10.1029/97JB03105>
- Fornari, D. J., Gallo, D. G., Edwards, M. H., Madsen, J. A., Perfit, M. R., & Shor, A. N. (1989). Structure and topography of the Siqueiros transform fault system: Evidence for the development of intra-transform spreading centers. *Marine Geophysical Researches*, *11*(4), 263–299. <https://doi.org/10.1007/BF00282579>
- Forsyth, D. W. (1993). Crustal thickness and the average depth and degree of melting in fractional melting models of passive flow beneath mid-ocean ridges. *Journal of Geophysical Research*, *98*(B9), 16,073–16,079. <https://doi.org/10.1029/93JB01722>
- Forsyth, D. W., & Wilson, B. (1984). Three-dimensional temperature structure of a ridge-transform-ridge system. *Earth and Planetary Science Letters*, *10*, 355–362. [https://doi.org/10.1016/0012-821X\(84\)90019-0](https://doi.org/10.1016/0012-821X(84)90019-0)
- Fox, C. G., Radford, W. E., Dziak, R. P., Lau, T.-K., Matsumoto, H., & Schreiner, A. E. (1995). Acoustic detection of a seafloor spreading episode on the Juan de Fuca Ridge using military hydrophone arrays. *Geophysical Research Letters*, *22*, 131–134. <https://doi.org/10.1029/94GL02059>
- Fox, P. J., Schreiber, E., Rowlett, H., & McCamy, K. (1976). The geology of the Oceanographer fracture zone: A model for fracture zones. *Journal of Geophysical Research*, *81*, 4117–4128. <https://doi.org/10.1029/JB081i023p04117>
- Francis, T. J. G. (1981). Serpentinization faults and their role in the tectonics of slow spreading ridges. *Journal of Geophysical Research*, *86*, 11,616–11,622. <https://doi.org/10.1029/JB086iB12p11616>
- Gallo, D. G., Fox, P. J., & Macdonald, K. C. (1986). A Sea Beam investigation of the Clipperton Transform Fault: The morphotectonic expression of a fast slipping transform boundary. *Journal of Geophysical Research*, *91*(B3), 3455–3467. <https://doi.org/10.1029/JB091iB03p03455>
- Gasparini, L., Bernoulli, D., Bonatti, E., Borsetti, A., Ligi, M., Negri, A., et al. (2001). Lower Cretaceous to Eocene sedimentary transverse ridge at the Romanche Fracture Zone and the opening of the equatorial Atlantic. *Marine Geology*, *176*(1–4), 101–119. [https://doi.org/10.1016/s0025-3227\(01\)00146-3](https://doi.org/10.1016/s0025-3227(01)00146-3)
- Gasparini, L., Bonatti, E., Borsetti, A. M., Capotondi, L., Cipriani, A., & Negri, A. (2017). Timing of transverse ridge uplift along the Vema transform (Central Atlantic). *Marine Geology*, *385*, 228–232. <https://doi.org/10.1016/j.margeo.2017.01.008>
- GEBCO Compilation Group (2019). GEBCO 2019 grid (<https://doi.org/10.5285/836f016a-33be-6ddc-e053-6c86abc0788e>).
- Giusti, M., Perrot, J., Dziak, R. P., Sukhovich, A., & Maia, M. (2018). The August 2010 earthquake swarm at North FAMOUS–FAMOUS segments, Mid-Atlantic Ridge: Geophysical evidence of dike intrusion. *Geophysics of Journal International*. <https://doi.org/10.1093/gji/ggy239/5040764>
- Grandin, R., Jacques, E., Necessian, A., Ayele, A., Doubre, C., Socquet, A., et al. (2012). Seismicity during lateral dike propagation: Insights from new data in the recent Manda Hararo–Dabbahu rifting episode (Afar, Ethiopia). *Geochemistry, Geophysics, Geosystems*, *12*, Q0AB08. <https://doi.org/10.1029/2010GC003434>
- Granot, R., & Dymant, J. (2015). The Cretaceous opening of the South Atlantic Ocean. *Earth and Planetary Science Letters*, *414*, 156–163. <https://doi.org/10.1016/j.epsl.2015.01.015>
- Gregg, P. M., Behn, M. D., Lin, J., & Grove, T. L. (2009). Melt generation, crystallization, and extraction beneath segmented oceanic transform form faults. *Journal of Geophysical Research*, *114*, B11102. <https://doi.org/10.1029/2008JB006100>
- Gregg, P. M., Lin, J., Behn, M. D., & Montési, L. G. J. (2007). Spreading rate dependence of gravity anomalies along oceanic transform faults. *Nature*, *448*(7150), 183–187. <https://doi.org/10.1038/nature05962>
- Gregory, E., Marjanović, M., Wang, Z., Singh, S. C. (2020). Structure and composition of large-offset Atlantic transform faults: An extreme example at the Romanche transform from wide-angle refraction data. EGU2020-10151, EGU General Assembly 2020.
- Grevemeyer, I., Ranero, C. R., & Ivandić, M. (2018). Structure of oceanic crust and serpentinization at subduction trenches. *Geosphere*, *14*(2), 395–418. <https://doi.org/10.1130/GES01537.1>

- Grevemeyer, I., Singh, S., Villinger, H., Papenberg, C., & Kaul, N. E. (2019). LITHOS-ILAB—Structure and evolution of the oceanic lithosphere, cruise no. MSM69, 14.11.2017–22.12.2017, Mindelo/Praia (Cape Verdes)–Mindelo (Cape Verdes), Cruise Report, Bonn, https://doi.org/10.2312/cr_msm69
- Grove, K., Grevemeyer, I., Singh, S., & Papenberg, C. (2019). Seismic structure of the St. Paul Fracture Zone near 18°W in the Atlantic Ocean—Evidence for a magmatic origin of crust. *Geophysical Research Abstracts*, Vol. 21, EGU2019-4770, 2019, EGU General Assembly 2019.
- Harmon, N., Rychert, C., Agius, M., Tharimena, S., Le Bas, T., Kendall, J. M., & Constable, S. (2018). Marine geophysical investigation of the Chain Fracture Zone in the equatorial Atlantic from the PI-LAB experiment. *Journal of Geophysical Research: Solid Earth*, *123*, 11,016–11,030. <https://doi.org/10.1029/2018JB015982>
- Hasselgren, E., Clowes, R. M., & Calvert, A. J. (1992). Propagating rift pseudofaults—Zones of crustal underplating imaged by multichannel seismic reflection data. *Geophysical Research Letters*, *19*, 485–488. <https://doi.org/10.1029/92GL00368>
- Hey, R., Duennbier, F. K., & Morgan, W. J. (1980). Propagating rifts on midocean ridges. *Journal of Geophysical Research*, *85*, 3647–3658. <https://doi.org/10.1029/JB085iB07p03647>
- Hey, R., & Vogt, P. (1977). Spreading centers jumps and sub-axial asthenosphere flow near the Galapagos hotspot. *Tectonophysics*, *37*, 41–52. [https://doi.org/10.1016/0040-1951\(77\)90038-5](https://doi.org/10.1016/0040-1951(77)90038-5)
- Hey, R. N., Sinton, J. M., Kleinrock, M. C., Yonover, R. N., Macdonald, K. C., Miller, S. P., et al. (1992). ALVIN investigation of an active propagating rift system, Galapagos 95.5°W. *Marine Geophysical Researches*, *14*(3), 207–226. <https://doi.org/10.1007/BF01270630>
- Hoof, E. E. E., Detrick, R. S., & Kent, G. M. (1997). Seismic structure and indicators of magma budget along the Southern East Pacific Rise. *Journal of Geophysical Research*, *102*(B12), 27,319–27,340. <https://doi.org/10.1029/97JB02349>
- Hoof, E. E. E., Detrick, R. S., Toomey, D. R., Collins, J. A., & Lin, J. (2000). Crustal thickness and structure along three contrasting spreading segments of the Mid-Atlantic Ridge 33.5°–35°N. *Journal of Geophysical Research*, *105*, 8205–8226. <https://doi.org/10.1029/1999JB900442>
- Hoof, E. E. E., Kleinrock, M. C., & Ruppel, C. (1995). Rifting of oceanic crust at Endeavor Deep on the Juan Fernandez microplate. *Marine Geophysical Researches*, *17*, 251–273. <https://doi.org/10.1007/BF01203465>
- Ito, G., & Behn, M. D. (2008). Magmatic and tectonic extension at mid-ocean ridges: 2. Origin of axial morphology. *Geochemistry, Geophysics, Geosystems*, *9*, Q09O12. <https://doi.org/10.1029/2008GC001970>
- Kahle, R., Tilmann, F., & Grevemeyer, I. (2016). Crustal structure and kinematics of the TAMMAR propagating rift system on the Mid-Atlantic Ridge from seismic refraction and satellite altimetry gravity. *Geophysical Journal International*, *206*, 1382–1397. <https://doi.org/10.1093/gji/ggw219>
- Karson, J., & Dewey, J. F. (1978). Coastal Complex, western Newfoundland: An Early Ordovician oceanic fracture zone. *Bulletin of the Geological Society of America*, *89*(7), 1037–1049.
- Karson, J. A., & Dick, H. J. B. (1983). Tectonics of ridge-transform intersections at the Kane fracture zone. *Marine Geophysical Researches*, *6*, 51–98. <https://doi.org/10.1007/BF00300398>
- Karson, J. A., Thompson, G., Humphris, S. E., Edmond, J. M., Bryan, W. B., Brown, J. R., et al. (1987). Along-axis variations in seafloor spreading in the MARK area. *Nature*, *328*, 681–685. <https://doi.org/10.1038/328681a0>
- Karson, J. A., Tivey, M. A., & Delaney, J. R. (2002). Internal structure of uppermost oceanic crust along the Western Blanco Transform Scarp: Implications for subaxial accretion and deformation at the Juan de Fuca Ridge. *Journal of Geophysical Research*, *107*(B9), 2181. <https://doi.org/10.1029/2000JB000051>
- Kastens, K., Bonatti, E., Caress, D., Carrara, G., Dauteuil, O., Frueh-Green, G., et al. (1998). The Vema Transverse ridge (Central Atlantic). *Marine Geophysical Researches*, *20*(6), 533–556. <https://doi.org/10.1023/A:1004745127999>
- Kearey, P., & Vine, F. J. (2002). *Global tectonics*. Australia: Blackwell Publishing.
- Keir, D., Hamling, I. J., Ayele, A., Calais, E., Ebinger, C. J., Wright, T. J., et al. (2009). Evidence for focused magmatic accretion at segment centers from lateral dike injection captured beneath the Red Sea rift of Afar. *Geology*, *37*, 59–62. <https://doi.org/10.1130/G25147A.1>
- Kleinrock, M. C., & Hey, R. N. (1989). Detailed tectonics near the tip of the Galapagos 95.5°W propagator: How the lithosphere tears and a spreading axis develops. *Journal of Geophysical Research*, *94*, 13,801–13,838. <https://doi.org/10.1029/JB094iB10p13801>
- Kruse, E. S., Tebbens, S. F., Naar, D. F., Lou, Q., & Bird, R. (2000). Comparisons of gravity anomalies at pseudofaults, fracture zones, and nontransform discontinuities from fast to slow spreading areas. *Journal of Geophysical Research*, *105*, 28,399–28,410. <https://doi.org/10.1029/2000JB900281>
- Kuo, B. Y., & Forsyth, D. W. (1988). Gravity anomalies of the ridge transform intersection system in the South Atlantic between 31 and 34.5°S: Upwelling centers and variations in crustal thickness. *Marine Geophysical Researches*, *10*, 205–232. <https://doi.org/10.1007/BF00310065>
- Lagabrielle, Y., Mameloukas-Frangoulis, V., Cannat, M., Auzende, J.-M., Honnorez, J., Mevel, C., & Bonatti, E. (1992). Vema Fracture Zone (central Atlantic): Tectonic and magmatic evolution of the median ridge and the eastern ridge-transform intersection domain. *Journal of Geophysical Research*, *97*(B12), 17,331–17,351. <https://doi.org/10.1029/92JB01086>
- Langseth, M. G., & Hobart, M. A. (1976). Interpretation of heat flow measurements in the Vema Fracture Zone. *Geophysical Research Letters*, *3*, 241–244. <https://doi.org/10.1029/GL003i005p00241>
- Larson, R. L., & Ladd, J. W. (1979). Evidence for the opening of the South Atlantic in the early Cretaceous. *Nature*, *246*, 209–212. <https://doi.org/10.1038/246209a0>
- Lay, T. (2019). Reactivation of oceanic fracture zones in large intraplate earthquakes? In *Transform plate boundaries and fracture zones* (pp. 89–104). Amsterdam, The Netherlands: Elsevier Inc. <https://doi.org/10.1016/B978-0-12-812064-4.00004-9>
- Le Voyer, M., Cottrell, E., Kelley, K. A., Brounce, M., & Hauri, E. H. (2015). The effect of primary versus secondary processes on the volatile content of MORB glasses: An example from the equatorial Mid-Atlantic Ridge (5°N–3°S). *Journal of Geophysical Research: Solid Earth*, *120*, 125–144. <https://doi.org/10.1002/2014JB011160>
- Ligi, M., Bonatti, E., Gasperini, L., & Poliakov, A. N. B. (2002). Oceanic broad multi-fault transform plate boundaries. *Geology*, *30*(1), 11–14. [https://doi.org/10.1130/0091-7613\(1990\)018%3C0886:ORPACO%3E2.3.CO;2](https://doi.org/10.1130/0091-7613(1990)018%3C0886:ORPACO%3E2.3.CO;2)
- Lin, J., & Phipps Morgan, J. (1992). The spreading rate dependence of three-dimensional mid-ocean ridge gravity structure. *Geophysical Research Letters*, *19*, 13–16. <https://doi.org/10.1029/91GL03041>
- Lin, J., Purdy, G. M., Schouten, H., Sempere, J.-C., & Zervas, C. (1990). Evidence from gravity data for focused magmatic accretion along the Mid-Atlantic Ridge. *Nature*, *344*, 627–632. <https://doi.org/10.1038/344627a0>
- Lonsdale, P. (1989). Segmentation of the Pacific-Nazca spreading center, 1°N–20°S. *Journal of Geophysical Research*, *94*, 12,197–12,225. <https://doi.org/10.1029/JB094iB09p12197>

- Lonsdale, P. (1994). Structural geomorphology of the eltanin fault system and adjacent transform faults of the Pacific-Antarctic plate boundary. *Marine Geophysical Researches*, *16*(2), 105–143. <https://doi.org/10.1007/BF01224756>
- Louden, K. E., & Forsyth, D. W. (1976). Thermal conduction across fracture zones and the gravitational edge effect. *Journal of Geophysical Research*, *81*(26), 4869–4874. <https://doi.org/10.1029/JB081i026p04869>
- Lowrie, A., Smoot, C., & Batiza, R. (1986). Are oceanic fracture zones locked and strong or weak? New evidence for volcanic activity and weakness. *Geology*, *14*(3), 242–245. [https://doi.org/10.1130/0091-7613\(1986\)14%3C242:AOFZLA%3E2.0.CO;2](https://doi.org/10.1130/0091-7613(1986)14%3C242:AOFZLA%3E2.0.CO;2)
- Ludwig, W. J., & Rabinowitz, P. D. (1980). Structure of Vema Fracture Zone. *Marine Geology*, *35*, 99–110. [https://doi.org/10.1016/0025-3227\(80\)90024-9](https://doi.org/10.1016/0025-3227(80)90024-9)
- Macdonald, K. C., Fox, P. J., Perram, L. J., Eisen, M. F., Haymon, R. M., Miller, S. P., et al. (1988). A new view of the mid-ocean ridge from the behaviour of ridge axis discontinuities. *Nature*, *335*, 217–225. <https://doi.org/10.1038/335217a0>
- Macdonald, K. C., Scheirer, D. S., & Carbotte, S. M. (1991). Mid-ocean ridges: Discontinuities, segments and giant cracks. *Science*, *253*, 986–994. <https://doi.org/10.1126/science.253.5023.986>
- Maia, M. (2018). Topographic and morphologic evidences of deformation at oceanic transform faults: Far-field and local-field stresses. In *Transform plate boundaries and fracture zones* (Chap. 3, pp. 61–87). Amsterdam, The Netherlands: Elsevier Inc. <https://doi.org/10.1016/B978-0-12-812064-4.00003-7>
- Maia, M., Sichel, S., Briais, A., Brunelli, D., Ligì, M., Ferreira, N., et al. (2016). Extreme mantle uplift and exhumation along a transpressive transform fault. *Nature Geoscience*, *9*(8), 619–623. <https://doi.org/10.1038/ngeo2759>
- Marjanović, M., Carbotte, S. M., Carton, H. D., Nedimović, M. R., Canales, J. P., & Mutter, J. C. (2018). Crustal magmatic system beneath the East Pacific Rise (8°20' to 10°10'N): Implications for tectonomagmatic segmentation and crustal melt transport at fast-spreading ridges. *Geochemistry, Geophysics, Geosystems*, *19*, 4584–4611. <https://doi.org/10.1029/2018GC007590>
- Marjanović, M., Carbotte, S. M., Nedimović, M. R., & Canales, J. P. (2011). Gravity and seismic study of crustal structure along the Juan de Fuca Ridge axis and across pseudofaults on the ridge flanks. *Geochemistry, Geophysics, Geosystems*, *12*, Q05008. <https://doi.org/10.1029/2010GC003439>
- Marjanović, M., Growe, K., Gregory, E., Singh, S., Grevemeyer, I., Vaddineni, V., et al. (2019). Variations in structural and thermal properties of the lithosphere across large fracture zones/transform fault in the equatorial Atlantic. Abstract [T41B-03] 2019 Fall Meeting, AGU, San Francisco, 9–13 Dec.
- Marjanović, M., Singh, S., Audhkhshi, P., & Mehouchi, F. (2015). Seismic reflection imaging of the lithosphere-asthenosphere boundary across the Atlantic Ocean. Abstract T41D-2926, 2015 Fall Meeting, AGU, San Francisco, California.
- Mauduit, T., & Dauteuil, O. (1996). Small-scale models of oceanic transform zones. *Journal of Geophysical Research*, *101*(B9), 20,195–20,209. <https://doi.org/10.1029/96JB01509>
- McClymont, A. F., & Clowes, R. M. (2005). Anomalous lithospheric structure of northern Juan de Fuca plate—A consequence of oceanic rift propagation? *Tectonophysics*, *406*, 213–231. <https://doi.org/10.1016/j.tecto.2005.05.026>
- Mehouchi, F., & Singh, S. C. (2018). Water-rich sublithospheric melt channel in the equatorial Atlantic Ocean. *Nature Geoscience*, *11*, 65–69. <https://doi.org/10.1038/s41561-017-0034-z>
- Menard, H. W. (1967). Extension of northeastern-Pacific fracture zones. *Science*, *155*, 72–74. <https://doi.org/10.1126/science.155.3758.72>
- Menard, H. W., & Atwater, T. (1969). Origin of fracture zone topography. *Nature*, *222*, 1037–1040. <https://doi.org/10.1038/2221037a0>
- Minshull, T. A., White, R. S., Detrick, R. S., Mutter, J. C., Buhl, P., & Morris, E. (1991). Crustal structure at the Blake Spur fracture zone from expanding spread profiles. *Journal of Geophysical Research*, *96*, 9955–9984. <https://doi.org/10.1029/91JB00431>
- Morgan, J. P., & Forsyth, D. W. (1988). Three-dimensional flow and temperature perturbations due to a transform offset: Effects on oceanic crustal and upper mantle structure. *Journal of Geophysical Research*, *93*(B4), 2955–2966. <https://doi.org/10.1029/JB093iB04p02955>
- Morgan, W. J. (1968). Rises, trenches, great faults, and crustal blocks. *Journal of Geophysical Research*, 1959–1982. <https://doi.org/10.1029/JB073i006p01959>
- Moulin, M., Arslanian, D., & Unternehr, P. (2010). A new starting point for the South and Equatorial Atlantic. *Earth Science Reviews*, *98*, 1–170. <https://doi.org/10.1016/j.earscirev.2009.08.001>
- Muller, M. R., Minshull, T. A., & White, R. S. (2000). Crustal structure of the Southwest Indian Ridge at the Atlantis II Fracture Zone. *Journal of Geophysical Research*, *105*, 25,809–25,828. <https://doi.org/10.1029/2000JB900262>
- Müller, R. D., Royer, J. Y., Cande, S. C., Roest, W. R., & Maschenkov, S. (1999). New constraints on the Late Cretaceous/Tertiary plate tectonic evolution of the Caribbean. *Sedimentary Basins of the World*, *4*, 33–59. [https://doi.org/10.1016/S1874-5997\(99\)80036-7](https://doi.org/10.1016/S1874-5997(99)80036-7)
- Müller, R. D., Sdrolias, M., Gaina, C., & Roest, W. R. (2008). Age, spreading rates and spreading symmetry of the world's ocean crust. *Geochemistry, Geophysics, Geosystems*, *9*, Q04006. <https://doi.org/10.1029/2007GC001743>
- Murton, B. J., & Gass, I. G. (1986). Western Limassol Forest complex, Cyprus: Part of an Upper Cretaceous leaky transform fault. *Geology*, *14*(3), 255–258. [https://doi.org/10.1130/0091-7613\(1986\)14%3C255:WLFCCP%3E2.0.CO;2](https://doi.org/10.1130/0091-7613(1986)14%3C255:WLFCCP%3E2.0.CO;2)
- Mutter, J. C., Detrick, R. S., & NAT Study Group (1984). Multichannel seismic evidence for anomalously thin crust at oceanic fracture zones. *Geology*, *12*, 534–537. [https://doi.org/10.1130/0091-7613\(1984\)12%3C534:MSEFAT%3E2.0.CO;2](https://doi.org/10.1130/0091-7613(1984)12%3C534:MSEFAT%3E2.0.CO;2)
- Nedimović, M. R., Carbotte, S. M., Harding, A. J., Detrick, R. S., Canales, J. P., Diebold, J. B., et al. (2005). Frozen magma lenses below the oceanic crust. *Nature*, *436*, 1149–1152. <https://doi.org/10.1038/nature03944>
- Parker, R. L. (1972). The rapid calculations of potential anomalies. *Geophysical Journal of the Royal Astronomical Society*, *31*, 447–455. <https://doi.org/10.1111/j.1365-246X.1973.tb06513.x>
- Parmentier, E. M., & Haxby, W. F. (1986). Thermal stresses in the oceanic lithosphere: Evidence from geoid anomalies at fracture zones. *Journal of Geophysical Research*, *91*(B7), 7193–7204. <https://doi.org/10.1029/JB091iB07p07193>
- Peirce, C., Reveley, G., Robinson, A. H., Funnell, M. J., Searle, R. C., Simão, N. M., et al. (2019). Constraints on crustal structure of adjacent OCCs and segment boundaries at 13°N on the Mid-Atlantic Ridge. *Geophysical Journal International*, *217*(2), 988–1010. <https://doi.org/10.1093/gji/ggz074>
- Pockalny, R. A. (1997). Evidence of transpression along the Clipperton Transform: Implications for processes of plate boundary reorganization. *Earth and Planetary Science Letters*, *146*, 449–464.
- Pockalny, R. A., Fox, P. J., Fornari, D. J., Macdonald, K. C., & Perfit, M. R. (1997). Tectonic reconstruction of the Clipperton and Siqueiros Fracture Zones: Evidence and consequences of plate motion change for the last 3 Myr. *Journal of Geophysical Research*, *102*(B2), 3167–3181. <https://doi.org/10.1029/96JB03391>
- Pockalny, R. A., Gente, P., & Buck, R. (1996). Oceanic transverse ridges: A flexural response to fracture-zone-normal extension. *Geology*, *24*(1), 71–74. [https://doi.org/10.1130/0091-7613\(1996\)024%3C0071:OTRAFR%3E2.3.CO;2](https://doi.org/10.1130/0091-7613(1996)024%3C0071:OTRAFR%3E2.3.CO;2)
- Potts, C. G., Calvert, A. J., & White, R. S. (1986). Crustal structure of Atlantic fracture zones—III. The Tydeman fracture zone. *Geophysical Journal of the Royal Astronomical Society*, *86*, 909–942. <https://doi.org/10.1111/j.1365-246X.1986.tb00668.x>

- Potts, C. G., White, R. S., & Loudon, K. E. (1986). Crustal structure of Atlantic fracture zones—II. The Vema fracture zone and transverse ridge. *Geophysical Journal of the Royal Astronomical Society*, *86*, 491–513. <https://doi.org/10.1111/j.1365-246X.1986.tb03840.x>
- Prigent, C., Warren, J. M., Kohli, A. H., & Teyssier, C. (2020). Fracture-mediated deep seawater flow and mantle hydration on oceanic transform faults. *Earth and Planetary Science Letters*, *532*, 115988. <https://doi.org/10.1016/j.epsl.2019.115988>
- Roland, E., Lizarralde, D., McGuire, J. J., & Collins, J. A. (2012). Seismic velocity constraints on the material properties that control earthquake behavior at the Quebrada-Discovery-Gofar transform faults, East Pacific Rise. *Journal of Geophysical Research*, *117*, B11102. <https://doi.org/10.1029/2012JB009422>
- Ryan, W. B. F., Carbotte, S. M., Coplan, J. O., O'Hara, S., Melkonian, A., Arko, R., et al. (2009). Global Multi-Resolution Topography synthesis. *Geochemistry, Geophysics, Geosystems*, *10*, Q03014. <https://doi.org/10.1029/2008GC002332>
- Sandwell, D. T. (1984). Thermomechanical evolution of oceanic fracture zones. *Journal of Geophysical Research*, *89*(B13), 11,401–11,413. <https://doi.org/10.1029/JB089iB13p11401>
- Sandwell, D. T., Müller, R. D., Smith, W. H. F., Garcia, E., & Francis, R. (2014). New global marine gravity model from Cryo-Sat-2 and Jason-1 reveals buried tectonic structure. *Science*, *346*(6205), 65–67. <https://doi.org/10.1126/science.1258213>
- Sandwell, D. T., & Schubert, G. (1982). Geoid height-age relation from SEASAT altimeter profiles across the Mendocino Fracture Zone. *Journal of Geophysical Research*, *87*(B5), 3949–3958. <https://doi.org/10.1029/JB087iB05p03949>
- Schilling, J.-G., Hanan, B. B., McCully, B., & Kingsley, R. H. (1994). Influence of the Sierra Leone mantle plume on the equatorial mid-Atlantic Ridge: A Nd-Sr-Pb isotopic study. *Journal of Geophysical Research*, *99*, 12,005–12,028. <https://doi.org/10.1029/94JB00337>
- Schilling, J. G., Ruppel, C., Davis, A. N., McCully, B., Tghe, S. A., Kingsley, R. H., & Lin, J. (1995). Thermal structure of the mantle beneath the equatorial Mid-Atlantic Ridge: Inference from the spatial variation of dredged basalt glass compositions. *Journal of Geophysical Research*, *100*, 10,057–10,076. <https://doi.org/10.1029/95JB00668>
- Sempéré, J.-C., Lin, J., Brown, H. S., Schouten, H., & Purdy, G. M. (1993). Segmentation and morphotectonic variations along a slow-spreading center: The Mid-Atlantic Ridge (24°00'N–30°40'N). *Marine Geophysical Research*, *15*, 153–200. [https://doi.org/10.1016/0012-821X\(94\)00259-2](https://doi.org/10.1016/0012-821X(94)00259-2)
- Singh, S. C. (2015). European Research Council funds 2D ultra-deep seismic reflection data acquisition across the Atlantic Ocean. *First Break*, *33*, 47–48.
- Sinha, M. C., & Loudon, K. E. (1983). The Oceanography fracture zone—I. Crustal structure from seismic refraction studies. *Geophysical Journal of the Royal Astronomical Society*, *75*, 713–736. <https://doi.org/10.1111/j.1365-246X.1983.tb05007.x>
- Skolotnev, S. G., Sanfilippo, A., Peyve, A. A., Muccini, F., Sokolov, S. Y., Sani, C., et al. (2020). Large-scale structure of the Doldrums multi-fault transform system (7–8°N equatorial Atlantic): Preliminary results from the 45th expedition of the *R/V A. N. Strakhov. Ofioliti*, *45*(1), 25–41.
- Sleep, N. H., & Biehler, S. (1970). Topography and tectonics at the intersections of fracture zones with central rifts. *Journal of Geophysical Research*, *75*, 2748–2752. <https://doi.org/10.1029/JB075i014p02748>
- Spencer, S., Smith, D. K., Cann, J. R., Lin, J., & McAllister, E. (1997). *Marine Geophysical Researches*, *19*(4), 339–362. <https://doi.org/10.1023/a:1004200411959>
- Stakes, D. S., Shervais, J. W., & Hopson, C. A. (1984). The volcanic-tectonic cycle of the FAMOUS and AMAR valleys, Mid-Atlantic Ridge (36°47'N): Evidence from basalt glass and phenocryst compositional variations for a steady state magma chamber beneath the valley midsections, AMAR 3. *Journal of Geophysical Research*, *89*, 6995–7028. <https://doi.org/10.1029/JB089iB08p06995>
- Thibaud, R., Gente, P., & Maia, M. (1998). A systematic analysis of the Mid-Atlantic Ridge morphology and gravity between 15°N and 40°N: Constraints of the thermal structure. *Journal of Geophysical Research*, *103*(24), 223–243. <https://doi.org/10.1029/97JB02934>
- Tolstoy, M., Harding, A., & Orcutt, J. (1993). Crustal thickness on the Mid-Atlantic Ridge: Bulls-eye gravity anomalies and focused accretion. *Science*, *262*, 726–729. <https://doi.org/10.1126/science.262.5134.726>
- Toomey, D. R., & Foulger, G. R. (1989). Tomographic inversion of local earthquake data from the Hengill-Grensdalur central volcano complex, Iceland. *Journal of Geophysical Research*, *94*, 17,497–17,510. <https://doi.org/10.1029/JB094iB12p17497>
- Tréhu, A. M., & Purdy, G. M. (1984). Crustal structure in the Orozco transform zone. *Journal of Geophysical Research*, *89*(B3), 1834–1842. <https://doi.org/10.1029/JB089iB03p01834>
- Tucholke, B. E., & Schouten, H. (1988). Kane Fracture Zone. *Marine Geophysical Researches*, *10*, 1–39. <https://doi.org/10.1007/BF02424659>
- U.S. Geological Survey (2016). Earthquake facts and statistics, accessed March 31, 2020 at URL: <https://earthquake.usgs.gov/earthquakes/eventpage/us20005i2p/executive>
- Vaddineni, V., Mehouchi, F., Singh, S., Grevemeyer, I., Carton, H., Marjanović, M., et al. (2019). Effects of Chain Transform Fault on the Lithosphere-Asthenosphere boundary [T43F-0517] to be presented at 2019 Fall Meeting, AGU, San Francisco, 9–13 Dec.
- Van Avendonk, H. J., Harding, A. J., Orcutt, J. A., & McClain, J. S. (1998). A two-dimensional tomographic study of the Clipperton transform fault. *Journal of Geophysical Research*, *103*(B8), 17,885–17,899. <https://doi.org/10.1029/98JB00904>
- Van Avendonk, H. J. A., Shillington, D. J., Holbrook, W. S., & Hornbach, M. J. (2004). Inferring crustal structure in the Aleutian island arc from a sparse wide-angle seismic data set. *Geochemistry, Geophysics, Geosystems*, *5*, Q08008. <https://doi.org/10.1029/2003GC000664>
- Vogt, P. R. (1974). Volcano spacing, fractures, and thickness of the lithosphere. *Earth and Planetary Science Letters*, *21*, 235–252. [https://doi.org/10.1016/0012-821X\(74\)90159-9](https://doi.org/10.1016/0012-821X(74)90159-9)
- West, B. P., Lin, J., & Christie, D. M. (1999). Forces driving ridge propagation. *Journal of Geophysical Research*, *104*, 22,845–22,858. <https://doi.org/10.1029/1999JB900154>
- White, R., McKenzie, D., & O'Nions, R. (1992). Oceanic crustal thickness from seismic measurements and rare earth element inversions. *Journal of Geophysical Research*, *97*(B13), 19,683–19,715. <https://doi.org/10.1029/92JB01749>
- White, R. S., Detrick, R. S., Mutter, J. C., Bum, P., Minshull, T. A., & Morris, E. (1990). New seismic images of oceanic crustal structure. *Geology*, *18*, 462–465. [https://doi.org/10.1130/0091-7613\(1990\)018%3C0462:NSIOOC%3E2.3.CO;2](https://doi.org/10.1130/0091-7613(1990)018%3C0462:NSIOOC%3E2.3.CO;2)
- Whitmarsh, R. B., & Calvert, A. J. (1986). Crustal structure of Atlantic fracture zones—I. The Charlie-Gibbs Fracture Zone. *Geophysical Journal of the Royal Astronomical Society*, *85*, 107–138. <https://doi.org/10.1111/j.1365-246X.1986.tb05174.x>
- Wilson, J. T. (1965). A new class of faults and their bearing on continental drift. *Nature*, *203*(207), 343–347. <https://doi.org/10.1038/207343a0>